PCCP

PAPER

View Article Online
View Journal | View Issue

Cite this: *Phys. Chem. Chem. Phys.*, 2024, **26**, 27189

Comprehensive characterization of waterlogged archaeological wood by NMR relaxometry, diffusometry, micro-imaging and cryoporometry

Valeria Stagno, *[ab] Otto Mankinen, [c] Sarah Mailhiot,[c] Ville-Veikko Telkki [c] and Silvia Capuani[b]

Received 8th July 2024,
Accepted 12th October 2024

DOI: 10.1039/d4cp02697g

rsc.li/pccp

Chemical, physical, and biological decay may partially or totally hide the historical and technological information carried by waterlogged wood. Investigation of the above-mentioned decay processes is essential to assess the wood preservation state, and it is important to find new methods for the consolidation and safeguarding of wooden archaeological heritage. A conventional method for assessing the wood preservation state is light microscopy. However, the method requires sample slicing, which is destructive and challenging when dealing with fragile and spongy submerged remains of heritage wood. To this end, a promising alternative non-destructive technique is proton nuclear magnetic resonance (^{1}H-NMR) which considers wood as a porous system. This work aimed to perform a comprehensive analysis of structures, porosity, water distribution, decay, and possible structural inclusions of three archaeological waterlogged wood fragments of the Roman age using NMR relaxometry, micro-imaging (μ-MRI), NMR diffusometry, and NMR cryoporometry. The results were compared with a similar analysis of the three contemporary wood samples of the same species. The multimodal approach presented in this study allowed us to cover all the dimensional scales of wood, from nanometers to sub-millimeters, and reconstruct the alteration of the entire archaeological wood fragment caused by degradation.

Introduction

Archaeological wood remains are essential for understanding past human activities and raw materials technology.[1] Under waterlogged conditions, the information carried by these remains may be partially hidden or lost due to physico-chemical and biological degradation, which induces an alteration of the wood structure depending on the properties of the wood species as well as environmental factors of the deposition site.[2–4] Beyond physico-chemical and biological decay, tunnelling and erosion bacteria may lead to a microbial process in the presence of oxygen and anoxic conditions, respectively.[4,5] Wood can also be attacked by soft-rot fungi when the oxygen level increases.[2,6] Erosion bacteria produce the destruction of the cell walls and pit membranes and the filling of cell lumina with decay products from the cell wall layers.[6,7] Along with the decay products, salts, and metals may be deposited within the wood depending on their concentration in water and the composition of the soil in which the object was buried.[8–11] The assessment of the wood preservation state, based on the investigation of the above-mentioned degradation processes, is important for the implementation of new methods and materials to consolidate and safeguard the wooden archaeological heritage.[12,13] For waterlogged archaeological wood, the main conservation practice implies the use of consolidating materials that penetrate in the wood microstructure and replace water.[14–19] Sometimes, these consolidants interact with the impurities (*i.e.*, salts and metals) stored in the archaeological wood remains, compromising their conservative effect.[14] Therefore, knowledge of porosity, water distribution, decay and possible structural inclusions in the wood is crucial for the choice of an appropriate consolidating product.

A conventional way for assessing the wood preservation state is light microscopy. This is an optical imaging technique classified as destructive, since it requires sampling a piece of wood[20] and manually cutting it into thin sections. When dealing with the waterlogged archaeological wood, the main limitations of light microscopy are related to the sample volume[21] and the fact that it is often used to provide qualitative images. The first limitation may be partially solved by selecting only one small sample in areas that would not affect the value of the object.[22] However, with conventional light microscopy, even a

---

[a] *Earth Sciences Department, Sapienza University of Rome, Piazzale Aldo Moro 5, 00185 Rome, Italy. E-mail: valeria.stagno@uniroma1.it; Tel: +39 0649913928*

[b] *National Research Council – Institute for Complex Systems (CNR-ISC) c/o Physics Department Sapienza University of Rome, Piazzale Aldo Moro 5, 00185 Rome, Italy*

[c] *NMR Research Unit, University of Oulu, Pentti Kaiteran katu 1, 90014 Oulu, Finland*

small sample is destroyed to obtain a thin section compromising its use for further analysis. Moreover, because of the brittle and spongy texture of archaeological waterlogged wood remains, obtaining good informative images by conventional light microscopy can be a challenging task. Alternatively, reflected light microscopy and confocal laser scanning microscopy techniques[23–25] may be used since they do not require a thin section but are based on the observation of the external surface of the wood remains. However, the water present within the sample and on its surface reflects light making the application of these techniques on the archaeological waterlogged wood very difficult.

In the field of heritage waterlogged wood conservation, recent works[20,26–33] have shown that a promising alternative technique to light microscopy is represented by proton nuclear magnetic resonance (^{1}H-NMR). It is based on the stimulation of nuclear spins by radiofrequency (RF) waves in the presence of a static magnetic field. Under these conditions, an electric signal (NMR signal) is received by the RF probe as an electromotive force. The NMR signal is proportional to the proton density and it decays exponentially in time because of transverse (spin–spin) relaxation processes caused by local oscillating fields due to molecular motion.[34] These local oscillating fields both affect the transverse relaxation, with a time constant T_2, and the longitudinal relaxation, with a time constant T_1.[35–39] However, because of the static magnetic field inhomogeneities, which contribute to the spins' dephasing, the effective transverse relaxation time is known as T_2*. Superimposing over the main static magnetic field time-dependent and controlled magnetic field gradients, NMR images and diffusion experiments are obtained.[36] As the NMR signal depends on several parameters, such as the relaxation times T_1, T_2, and T_2* and the diffusion coefficient D, it is possible to perform a multiparametric and multimodal investigation of the wood object acquiring both non-imaging and imaging experiments. MR images weighted on one of the above-mentioned parameters provide a semi-quantitative and direct observation of the wood structure and the measurement of these parameters, by means of NMR experiments based on the signal analysis, allows the quantitative and indirect inspection of the physico-chemical and physiological aspects of the wood. Importantly, NMR is a non-destructive technique that allows the preservation of the wood sample for further analyses. All the aforementioned NMR techniques have already been used to study ancient wood.[9,26,40–44] However, magnetic resonance imaging (MRI) and diffusion NMR techniques do not allow the investigation at the sub-micrometer and nanometer scale, which is the dimensional scale characteristic of the cell wall which is the wood constituent most affected by degradation processes. With conventional diffusion techniques, the detection limit is essentially related to the diffusion length which in the Stejskal–Tanner model is set around 10 microns.[45,46] Also, micro-imaging (μ-MRI), when performed using strong magnetic field gradients, allows a maximum linear resolution of about 10 μm.[29] On the other hand, relaxation times may provide indirect information about the nanometer scale features but they are also sensitive to paramagnetic ions that reduce the relaxation constants and cause the appearance of unrealistic pore distributions in mathematical models used.[28,47] In this scenario, NMR cryoporometry represents a non-destructive method to also investigate the cell wall scale and, combined with other NMR techniques, cover the entire wood dimensional scale.[44,48]

One limitation of high-field NMR and microscopic MRI is that the sample size is typically limited to a few millimeters or to a few centimeters depending on the instrument. However, surfaces of larger cultural heritage wood samples can be studied using low-field, portable single-sided NMR devices up to a couple of centimeters depth. Previous works[28,49–55] have shown that it is possible to perform relaxometry and diffusometry experiments with a single-sided NMR instrument without sampling the wood artwork. Nevertheless, these mobile devices are characterized by highly inhomogeneous magnetic fields and are not equipped with either imaging gradients or a cooling system. Therefore, despite allowing studies on unlimited sample sizes outside a laboratory, portable NMR has lower resolution and does not enable micro-imaging and cryoporometry measurements.

In this work, three waterlogged archaeological wood samples (V century AD) were studied using a combination of advanced NMR techniques. The three ancient wood samples were identified as common spruce (*Picea abies* Karst.), sweet chestnut (*Castanea sativa* Mill.), and maple (*Acer* L.), and their preservation state was already investigated using conventional light microscopy in our previous work.[28] The evaluation of decay was obtained by both normal and polarized light microscopy. A strong microbial decay was observed for spruce wood, which was associated with both cellulolytic bacteria and fungi. This decay resulted in a layer of dark-coloured substance, formed by erosion residual wood products, which appeared mainly in the secondary wall of latewood tracheids, facing the cell lumen. Polarized light microscopy highlighted the well-preserved structure of compound middle lamellae and secondary cell walls. Conversely, the inner part of the secondary walls was converted into an amorphous substance. A fungal attack was testified by the presence of hyphae passing through the cells and typical soft rot erosion tunnels. Moreover, inclusions were observed in both earlywood and latewood vessels of the chestnut wood and in some cases small vessels were completely obstructed. These black-coloured inclusions were attributed to iron–tannin precipitates.[8,9] A generalized detachment and loss of fibre secondary walls was also observed in chestnut, whereas in the maple wood no complete cell wall detachment was seen. Nevertheless, the weak and spongy consistency of the maple wood indicated a significant decay, and the thinning of the fibre cell wall as well as the presence of spores and residues of fungal hyphae in the cellular lumens were observed.

This work aimed to obtain a comprehensive analysis of archaeological waterlogged wood structures, along with their porosity, water distribution, decay, and potential structural inclusions, combining four advanced NMR techniques: relaxometry, micro-imaging, diffusometry, and cryoporometry. To this end, the three archaeological wood fragments of the Roman age were compared with three contemporary wood samples of the same species. The multi-analytical approach presented in this study allowed us to cover all the dimensional scales of wood, from nanometers to millimeters, and reconstruct the state of conservation of the entire archaeological wood fragment. The results obtained from the NMR protocol presented in this work were interpreted with the support of the results obtained from decay evaluation by light microscopy carried out in our previous work.[28]

Experimental

Materials

Three small fragments were collected from three archaeological wood poles of a wooden pier dated to the Roman age (V century AD) and recovered in 2018 in the archaeological excavation area of the ancient harbor of Neapolis (Naples, Italy).[56,57] Their botanical species were identified in previous works[57–62] as common spruce (*Picea abies* Karst.), sweet chestnut (*Castanea sativa* Mill.) and maple (*Acer* L.). These wood samples were waterlogged and well preserved in the seawater of Naples (Mediterranean Sea). After the collection, the samples were kept in sealed containers full of distilled water. Moreover, three modern wood samples belonging to the same botanical species of the three ancient wood samples were used for comparison. All six wood samples (three ancient kinds of wood samples and three modern kinds of wood samples) had cylinder-like shapes of height 1 cm and diameter of less than 1 cm so that they could be inserted into the 10 mm NMR tube. Before starting the NMR measurements, the three modern wood samples were soaked with distilled water until complete saturation (corresponding to the sinking of the sample) and maintained in test tubes full of distilled water. During the relaxometry, diffusometry and cryoporometry experiments, all six samples were inserted without water in the NMR tube that was sealed with Parafilm to prevent the wood dehydration. Conversely, during μ-MRI acquisitions, the samples were inserted in the NMR tube with water and sealed with Parafilm to prevent water evaporation.

Methods

Relaxometry. The spin–lattice relaxation time (T_1) and the spin–spin relaxation time (T_2) were measured with TopSpin 3.0 software using a Bruker-Avance III spectrometer with a ^{1}H resonance frequency of 300 MHz and a 7.04 T magnetic field strength. For the T_1 acquisition, the saturation-recovery (SR) sequence[63] was used instead of the inversion-recovery (IR)[64] to avoid the effect of radiation damping.[65] The recovery time varied from 10 μs to 10 s in 128 points, the repetition time (TR) was 10 s, and the number of scans (NS) was 4. T_2 measurements were performed with the Carr–Purcell–Meiboom–Gill (CPMG) sequence[66] using an echo-time (TE) of 0.5 ms, and number of echoes of 10 000; all the echoes were collected in a single transient, TR = 8 s, and NS = 4.

Micro-imaging. High-resolution images were obtained using a Bruker-Avance 400 MHz spectrometer with a 9.4 T magnetic field. A 10 mm micro-imaging probe equipped with high-performance and high-strength magnetic field gradients was mounted and the maximum gradient strength was 1200 mT m^{-1} with a rise time of 100 μs. Three images along the three anatomical directions of the wood, which correspond to three MRI virtual sections, were acquired for each wood sample. In this way, a complete virtual histology, composed of one cross-section and two longitudinal sections, similar to that traditionally carried out by light microscopy, was obtained. The three images/virtual slices were oriented as follows: perpendicular to the wood grain (transversal section), tangent to the annual ring boundary (tangential section), and parallel to the wood ray/perpendicular to the annual ring boundary (radial section). All the MRI experiments were acquired using ParaVision 5.1 software, which allowed us to set and control the acquisition parameters, such as the number of scans (NS), number of slices (N° slices), slice thickness (STK), field of view (FOV), image matrix (MTX), in-plane resolution (R), and echo time/repetition time ratio (TE/TR). The FOV and MTX were chosen equal in both image dimensions. After some tests, the T_2*-weighting (T_2*-w) of images turned out the optimal solution for all the wood samples except for the ancient chestnut for which, instead, the T_2-weighted (T_2-w) images provided a better discrimination among different tissues and less image artifacts. The T_2*-w images were acquired using either a gradient echo fast imaging (GEFI) sequence[67] or a mic-flash sequence,[68] whereas the T_2-w images were acquired using a multi-slice multi echo (MSME) sequence.[69] All the acquisition parameters and the sequences used were chosen to take into account the specific structural characteristics of each wood type and their degree of preservation (*e.g.*, the presence of impurities that can cause artifacts on the image), which were previously assessed in our work.[28] The MRI protocols used for the ancient wood samples are reported in Table 1, while those used for the modern wood samples are in Table 2.

Diffusometry. A pulsed gradient stimulated echo (PGSTE) sequence[70] was used to investigate the water diffusion in each wood sample with a 400 MHz spectrometer and the same probe was used for μ-MRI experiments. The PGSTE signal was obtained using a TR of 5 s, a TE of 5 ms, a diffusion gradient pulse length (δ) of 3 ms, and 32 steps of the gradient strength (g), from 26 to 1210 mT m^{-1}, for each diffusion time (Δ). The following Δ values were selected according to the different wood morphologies and longitudinal relaxation times T_1, so that $\Delta < T_1$[34,71]: 40–80–120–160–200–300–400–600–800–1000 ms. The diffusion gradient was activated along the x direction, *i.e.*, perpendicular to the wood grain or the vessel/tracheid main axis corresponding to the tangential direction of the wood. The b-value, which is defined as $b = \gamma^2 g^2 \delta^2 (\Delta - \delta/3)$, ranged from a minimum of 1.6×10^7 s m^{-2} to a maximum of 9.5×10^{11} s m^{-2}.

Cryoporometry. A 300 MHz Bruker-Avance III spectrometer with a 7.04 T field strength and a cooling system with a 1000 L h^{-1} airflow was used to perform the CPMG series over the temperature range of 25.4 K. The temperature was increased in 84 steps of 0.3 K from a minimum of 260.0 K to a maximum of 285.4 K. The experiment series was set using the TReNDS acquisition script[72] in TopSpin 3.5 software. At the beginning of the temperature series, the sample temperature

Table 1 Acquisition parameters used to obtain high-resolution images of ancient spruce, ancient chestnut, and ancient maple samples. T_2*-w images were obtained using a GEFI sequence, whereas T_2-w images using an MSME sequence

Wood sample	Ancient spruce			Ancient chestnut			Ancient maple		
Image weighting	T_2*-w			T_2-w			T_2*-w		
Slice orientation	Transversal	Tangential	Radial	Transversal	Tangential	Radial	Transversal	Tangential	Radial
TE/TR (ms)	5.5/500	5/1500	5/1500	2.8/2000	2.6/2000	2.6/2000	5/2000	4/2000	4/2000
NS	256	128	128	256	256	256	128	128	128
No of slices	10	10	10	10	10	10	10	10	10
STK (μm)	200	300	300	250	250	250	250	250	250
FOV (cm)	0.9	0.9	0.9	0.8	1.1	1.1	0.8	1.3	1.1
MTX	1024	512	512	512	512	512	512	512	512
R (μm^2)	9 × 9	18 × 18	18 × 18	16 × 16	21 × 21	21 × 21	16 × 16	25 × 25	21 × 21

Table 2 Acquisition parameters used to obtain high-resolution images of modern spruce, modern chestnut, and modern maple samples. Images were obtained using a GEFI sequence for spruce and a mic-flash sequence for chestnut and maple

Wood sample	Modern spruce			Modern chestnut			Modern maple		
Image weighting	T_2*-w			T_2*-w			T_2*-w		
Slice orientation	Transversal	Tangential	Radial	Transversal	Tangential	Radial	Transversal	Tangential	Radial
TE/TR (ms)	5.1/800	4.9/800	4.9/800	2.7/1000	2.6/1000	2.6/1000	2.7/1000	2.5/1000	2.7/1000
NS	100	128	128	256	256	256	256	256	256
No of slices	4	5	5	3	3	3	3	3	3
STK (μm)	300	250	250	300	300	300	300	300	300
FOV (cm)	0.8	1.0	1.0	0.9	1.2	1.15	0.9	1.2	1.2
MTX	1024	1024	1024	512	512	512	512	512	512
R (μm^2)	8 × 8	10 × 10	10 × 10	18 × 18	23 × 23	22 × 22	18 × 18	23 × 23	23 × 23

was left to stabilize at the lowest temperature for 2 h, then the heating rate was kept at a constant value by applying an appropriate temperature stabilization delay of 5 min K^{-1} before each experiment. The parameters in the CPMG experiments are TE = 300 μs, 1000 echoes, NS = 64, and TR = 10 s.

Data processing. The mean size of the characteristic porous elements of each wood type was obtained from the post-processing of the μ-MR images using ImageJ software. At least 10 counts were selected for each characteristic range of the pore size and its mean value was estimated. The diffusion coefficient (D) and the relaxation time T_1 and T_2 distributions were reconstructed in MATLAB using the inverse Laplace transform (ILT) method.[73–76] Especially, in the case of diffusion, this approach turned out to be preferable and more robust compared to curve fitting. This is due to ILT not requiring any assumption on the number of components while it is necessary for curve fitting. As wood is a complex heterogenous system, the number of components may vary between different diffusion measurements in the same sample due to relaxation filtering effects which are pronounced when the observation time Δ is increased. The ILT parameters were first evaluated to find robust ones and then the same parameters were used over the whole sample set. The diffusion coefficient values were then plotted as a function of the diffusion time Δ.

Since wood is a complex biological system, water diffusion is restricted and shows different behaviours depending on the observation time (Δ). At short Δ, *i.e.* when $L \gg \sqrt{D_0\Delta}$, where L is the length scale to probe the material structure or the typical pore size, $D(\Delta)$ depends on the surface-to-volume ratio S/V[77–81] according to the following equation:

$$\frac{D(\Delta)}{D_0} = 1 - \frac{S}{V}\frac{4}{9\sqrt{\pi}}\sqrt{D_0\Delta}, \qquad (1)$$

where S is the surface area of the pores, V is the volume of the pores, and D_0 is the diffusion coefficient of bulk water (2.2×10^{-9} m^2 s^{-1}). The surface-to-volume ratio was calculated by fitting eqn (1) to the initial part of D *vs.* Δ data for all the wood samples. Then, from S/V, the pore diameter (d) was calculated by assuming a spherical geometry. In a totally confined geometry, the mean square displacement is bounded at long time by the size of the confining pore L, and as Δ approached infinity, D approaches zero.[78,81] On the other hand, if the pores are interconnected, with long Δ values $\frac{D(\Delta)}{D_0}$, an asymptotic value approaches

$$D(\Delta \to \infty)/D_0 = 1/\tau, \qquad (2)$$

where τ is the tortuosity of pore space.[78–81] The tortuosity is an intrinsic property of a porous material that reflects the connectivity degree of the porous network.[79,82,83] However, the diffusion time that can be probed by NMR in a PGSTE experiment is limited by the relaxation time T_1, and the asymptotic limit cannot be necessarily reached. Therefore, Padé approximation was introduced to interpolate between the short-time behaviour (eqn (1)) and the long-time asymptotic value $1/\tau$:[78,80,81,84]

$$\frac{D(\Delta)}{D_0} = 1 - \left(1 - \frac{1}{\tau}\right) \times \frac{c\sqrt{\Delta} + (1 - 1/\tau)\Delta/\theta}{(1 - 1/\tau) + c\sqrt{\Delta} + (1 - 1/\tau)\Delta/\theta} \qquad (3)$$

where $c = \left(\frac{4}{9\sqrt{\pi}}\right)\left(\frac{S}{V}\right)\sqrt{D_0}$ and θ is a scaling constant proportional to the pore size.[78,84,85] This approximation was used to obtain the tortuosity for chestnut and maple samples. Since several diffusion components, D, were measured in each wood sample, for each D component, a tortuosity value was computed using either eqn (2) or eqn (3) and then an average tortuosity weighted on D populations was obtained.

In NMR cryoporometry, the melting point of a substance confined to a small pore is lower than that of a bulk substance, according to the Gibbs–Thomson equation:[44,86]

$$\Delta T = T_0(\text{bulk}) - T(\text{pore}) = \frac{K}{R} \tag{4}$$

where T_0(bulk) is the melting point of the bulk substance and T(pore) is the melting point of the substance confined in a pore with a radius R. K is a constant characteristic of the substance, in our case K = 30 K nm, which corresponds to the value experimentally determined for water absorbed in controlled pore glasses.[87] The intensity of the NMR signal is proportional to the volume of the pores containing the molten liquid at a given temperature and the pores size distribution is given by the following equation:[44,88–90]

$$P(R) = \frac{K}{R^2}\frac{\mathrm{d}I}{\mathrm{d}T} \tag{5}$$

where R is the pore radius and dI/dT is the derivative of the NMR signal intensity *vs.* the temperature curve. However, with the experimental setup used in this study, which is intrinsically limited by instrumental characteristics, at the lowest temperature (T = 260 K), there is still an observable signal indicating that the smallest nanoscale pores are not frozen yet. Therefore, we cannot report reliable pore size distributions. Nevertheless, the measured CPMG experiments over the temperature range were analysed with the ILT method, so that individual water components could be separated. Indeed, in the CPMG sequence, the echo time was much longer than the T_2 relaxation time of the solid wood and ice, but much shorter than T_2 of bound and free water.[48] In all cases, it was possible to distinguish the bound water signal (BW), water signal corresponding to micropore water (MP) and then with higher T_2, earlywood tracheid/vessel lumens (EW) and latewood tracheid/vessel lumens (LW).[48] According to literature, the moisture components of few millisecond relaxation times are usually associated with bound water in cell walls, and the other components with longer relaxation times, about 10–1000 ms, are associated with free water in bigger voids such as cell lumens.[91–95] Each signal was integrated separately and plotted against temperature for further examination. Moreover, the relative amount of bound water in pores with a size of below 8 nm was calculated from the ratio of the signal intensities measured at 265 K and above the bulk melting point (273 K).[96] This analysis is based on the fact that, according to eqn (4), only water in pores with their size of below 8 nm is unfrozen at 265 K, while above 273 K all water is unfrozen.

Results and discussion

Micro-imaging

Direct observation of the microstructure of our six wood samples was obtained by μ-MRI. Due to the finite echo time (2.5–5.5 ms, see Tables 1 and 2), the water components with the shortest T_2 values ($T_2 \leq$ TE) are filtered out from the images. Indeed, according to previous works,[9,10,26,27] the contrast of μ-MR images provides important information: areas with light image voxels correspond to wood structural damages, such as holes and cavities, filled with water; areas characterized by dark image voxels indicate the accumulation of decomposed organic materials and/or heavy metals, lacking the signal due to the lack of water and fast relaxation; rounded black and large spots suggest the presence of gas bubbles due to the gas emissions of infesting microorganisms (*e.g.*, fungi). The wood morphology is discussed separately for spruce, chestnut, and maple in the following sections.

Spruce

In Fig. 1, microscopic MR images of both the modern and the ancient spruce are shown, revealing their anatomies. The upper row (a, b, and c) of Fig. 1 displays images of the modern spruce, while the lower row (d, e, and f) shows images of the ancient spruce. In Fig. 1b, the presence of a black area (light blue arrow) in the upper part of the sample is due to the incomplete water filling of the wood structure, but it is not attributable to any decay process since it disappeared during the acquisition while the sample remained immersed in water in the NMR tube. Conversely, in all the MR images of the modern spruce, many black spots (red arrows), associated with a low water content and short T_2, are seen along the sample border, which are due to both the difference in the magnetic susceptibility and the presence of infest microorganisms. From the comparison among the MR images of the modern and the ancient spruce, the first thing to notice is the presence of many more artifacts and black spots (red arrows) in the ancient wood images. These are due to strongly degraded areas with bacteria, fungi, and paramagnetic inclusions.[9,28] Because most of the artifacts and black spots are located along the rays and on the sample border (red arrows), as visible in the transversal and tangential sections (Fig. 1d and e), we can conclude that these structures were heavily degraded. In these areas, characterized by dark voxels, the NMR signal is weak because of the lack of water or the very short T_2. Another notable difference is seen in the resin channels (green circles): those of the modern spruce appear with black image voxels and short T_2, whereas those of the ancient spruce are characterized by brighter voxels and long T_2. This indicates that resin was lost from the resin channels of the archaeological wood sample and replaced by water. Moreover, on average, the measured resin channels in the modern spruce have a diameter of around 75 μm and in the ancient spruce around 100 μm.

Chestnut

Fig. 2 shows the MRI-based virtual histology of both modern and ancient chestnuts. The modern chestnut images are displayed in

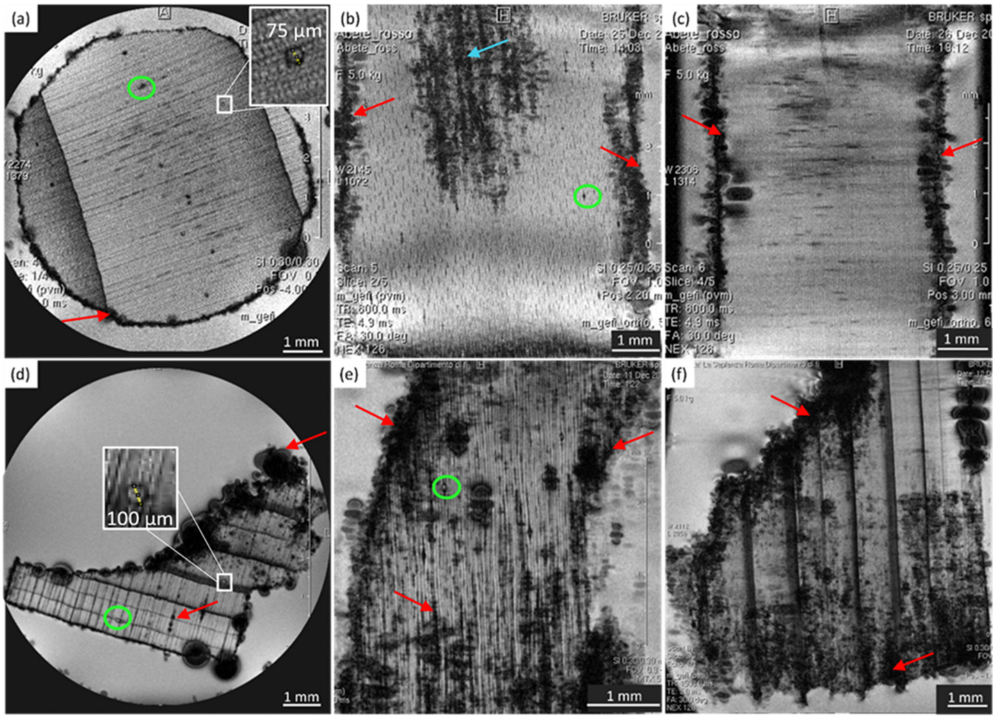

Fig. 1 Complete virtual histology of the modern spruce (a)–(c) and the ancient spruce (d)–(f) obtained by MRI: (a) and (d) the transversal sections, (b) and (e) the tangential sections and (c) and (f) the radial sections. Green circles indicate the resin channels; red arrows indicate the black spots and image artifacts; light blue arrow points to a region with incomplete water saturation.

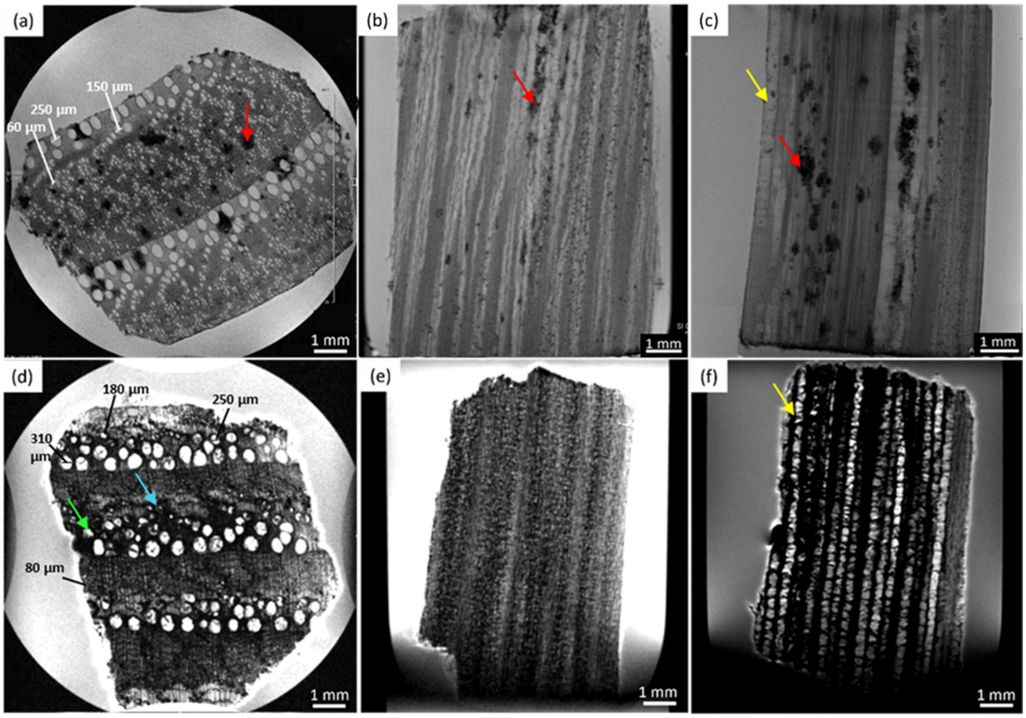

Fig. 2 Complete virtual histology of the modern chestnut (a)–(c) and the ancient chestnut (d)–(f) obtained by MRI: (a) and (d) the transversal sections, (b) and (e) the tangential sections and (c) and (f) the radial sections. Red arrows indicate the extractive accumulations; yellow arrows indicate the vessels length with or without inclusions; green arrow points to a partially obstructed vessel and light blue arrow to a totally obstructed vessel.

the upper row (a)–(c), while the ancient chestnut images are in the lower row (d)–(f). The MR sections acquired on the modern chestnut are characterized by a marked difference in the image contrast if compared with those acquired on the ancient chestnut.

The archaeological chestnut wood exhibits a very dark contrast throughout the MR images, which hides its typical porous-ring structure[60] and some regions appear with rather dark voxels associated with a low water content and short T_2. Indeed, only large pores characterized by bright voxels and long T_2 are fully resolved and they can be identified as vessels of the earlywood, while smaller vessels of the latewood, characterized by less bright voxels and shorter T_2, are only partially visible. Conversely, in the modern chestnut image, the porous-ring structure is clearly visible and it is characterized by pores with voxels of different brightness associated with different T_2 values, corresponding to vessels of different sizes, and a background with darker voxels and shorter T_2, associated with parenchyma, rays and fibres. Three and four main sizes of vessels can be measured, respectively, on the transversal section of the modern and ancient chestnuts, as highlighted in Fig. 2a and d. On average, the vessel sizes, when measured along the tangential direction, are around 295 ± 31, 139 ± 33 and 60 ± 16 μm for the modern chestnut and around 355 ± 45, 263 ± 10, 170 ± 22 and 83 ± 19 μm for the ancient chestnut. Furthermore, it is worth noting that modern chestnut vessels have an elongated shape characterized by a different diameter if measured along the tangential or the radial direction; instead, the ancient chestnut vessels exhibit a more circular shape. Transversal, tangential, and radial sections of the modern chestnut (Fig. 2a–c) show the presence of regions with black voxels and very short T_2 (red arrows) corresponding to the accumulation of extractives in which this wood type is naturally rich. Vessels, instead, appear almost totally free of inclusions in the modern chestnut and partially (green arrow) or totally (light blue arrow) obstructed in the ancient chestnut. The strong change in the image contrast between the modern and the ancient wood samples suggests a heavy degradation of the archaeological sample with the accumulation of inclusions and iron-impurities[9] both in the parenchyma and in the vessel lumens, as already highlighted in our previous work.[28] Moreover, the presence of inclusions can also be seen along the vessels in the radial section of the ancient chestnut (the yellow arrow in Fig. 2f) which, in contrast, are not present along vessels of the modern chestnut (the yellow arrow in Fig. 2c).

Maple

In Fig. 3, the MRI-reflected morphology of the modern and the ancient maple wood samples can be observed. The modern maple images are displayed in the upper row (a)–(c), while the ancient maple images are in the lower row (d)–(f). According to our previous work,[28] in which the assessment of the conservation state of these three archaeological wood samples was obtained by light microscopy, the ancient maple wood is better preserved than the ancient spruce and chestnut samples. Indeed, only a few black artifacts can be seen on the MR images (red arrows). For comparison, we used a piece of modern maple coming from a branch of the maple tree that for this reason has a different morphology in the center of the wood piece. However, the outermost zone well represents the typical diffuse porous-ring structure of the maple characterized by vessels with bright voxels and long T_2 and a background with darker voxels and shorter T_2 associated with parenchyma, rays and fibers. On average, vessels measured on the modern maple have a

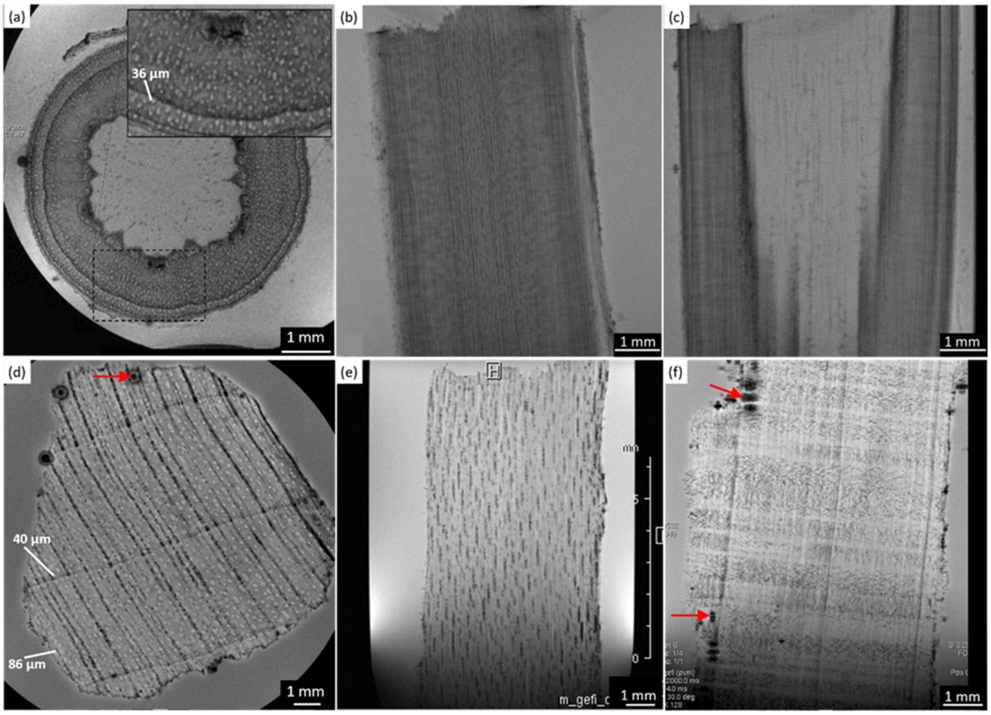

Fig. 3 Complete virtual histology of the modern maple (a)–(c) and ancient maple (d)–(f) obtained by MRI: (a) and (d) the transversal sections, (b) and (e) the tangential sections and (c) and (f) the radial sections. Red arrows indicate image artifacts associated with the presence of decay phenomena. The modern maple sample was taken from a branch.

diameter of 36 ± 8 μm, whereas vessels of the ancient maple are characterized by two different sizes of around 86 ± 10 μm and 40 ± 4 μm. In the ancient maple, the red arrows indicate the image artifacts that are usually produced by the presence of infest microorganisms.[6,9,28,47] These artifacts were not noticed in the modern maple images.

Relaxometry

The results obtained from the relaxometry analysis are discussed separately for spruce, chestnut, and maple in the following sections, where the T_1 and T_2 peaks shown in Fig. 4 have been interpreted and assigned to different water populations associated with characteristic wood structures. Peak assignments to wood anatomical elements are summarized in Table 3. On average, the ancient wood samples include more relaxation components than their modern counterparts.

Spruce

In Fig. 4a, the modern spruce has only two T_1 components and the ancient spruce presents three different T_1 components

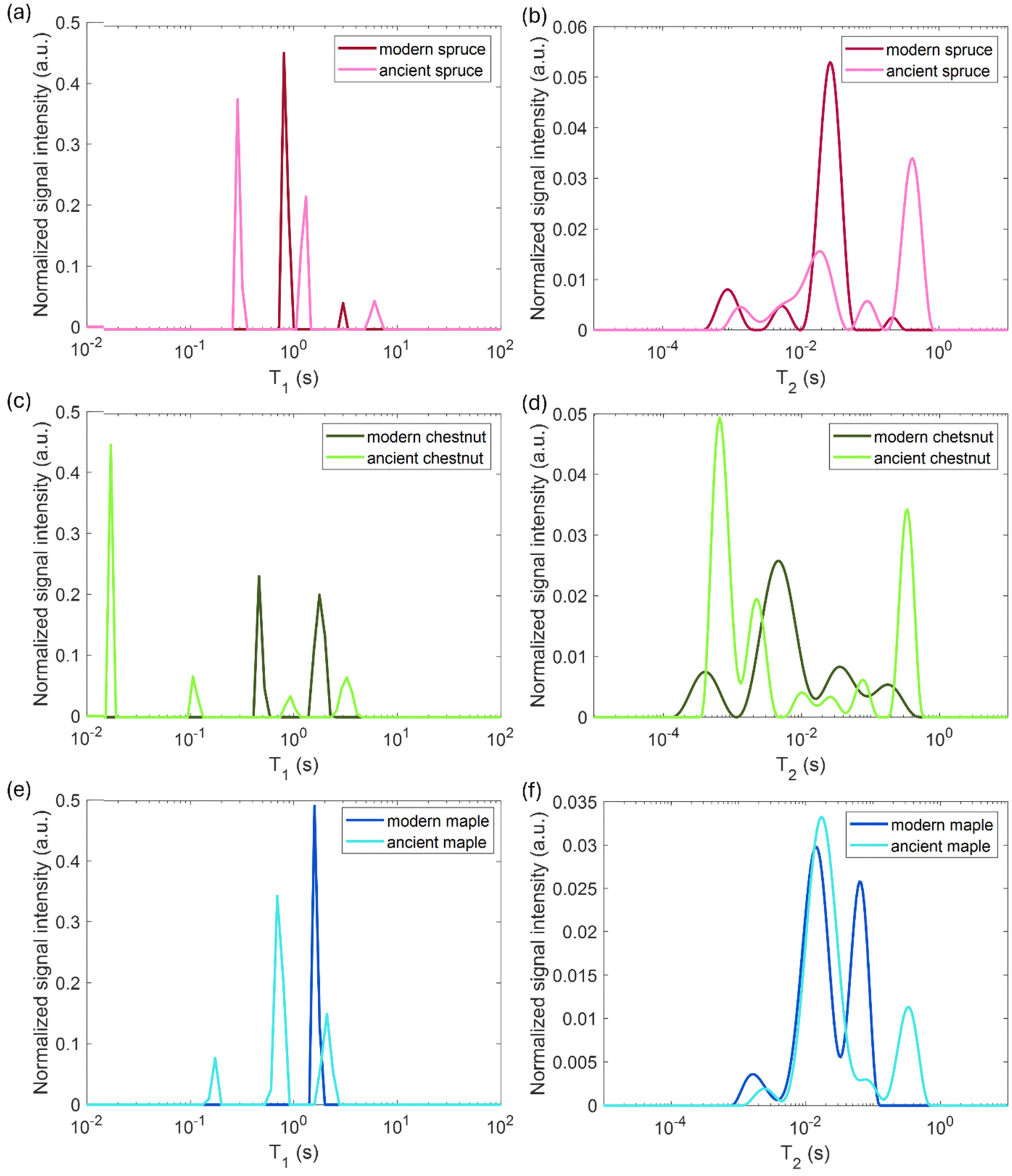

Fig. 4 (a), (c) and (e) Spin–lattice relaxation time (T_1) and (b), (d) and (f) spin–spin relaxation time (T_2) distributions of modern and ancient spruce (a) and (b), chestnut (c) and (d) and maple (e) and (f) samples.

Table 3 T_1 and T_2 peaks assignment for the six wood samples along with their probabilities P_1 and P_2

Wood specimen	T_1 (ms)	P_1 (%)	T_2 (ms)	P_2 (%)	Assignment
Modern spruce	3000	9	200	4	Water on the sample surface
	800	91	27	78	EW tracheids
			5	7	LW tracheids
			0.9	12	Cell walls
Ancient spruce	6000	7	—	—	Water on the sample surface
	1300	34	400	52	Large voids due to wood decay/empty resin channels
	300	59	97	9	Large EW tracheids
			18	24	EW tracheids
			5	8	LW tracheids
			1.4	7	Cell walls
Modern chestnut	1800	46	175	11	Vessels ~ 140–300 μm
			33	18	Vessels ~ 60 μm
	500	54	5	55	Fibres, parenchyma
			0.4	16	Cell walls
Ancient chestnut	3000	11	350	29	Vessels ~ 260–350 μm
	900	6	78	5	Vessels ~ 170 μm
			26	3	
	100	11	10	3	Vessels ~ 80 μm
	20	73	2	17	Cell walls
			0.6	42	Fibres, parenchyma
Modern maple	1600	100	70	44	Vessels ~ 36 μm
			15	50	Fibres, parenchyma
			1.5	6	Cell walls
Ancient maple	2100	26	350	23	Vessels ~ 86 μm
	700	60	78	6	Vessels ~ 40 μm
			16	67	Fibres, parenchyma
	200	13	2.3	4	Cell walls

where one of the components has significantly shorter T_1 than the components of the modern spruce sample. Both the modern and ancient spruce samples show a small (7–9% of the total intensity) peak at very long T_1 = 3 and 6 s, respectively. These T_1 peaks, along with the weak T_2 component around 200 ms observed only in the modern spruce, can be attributed to excess water stored in the NMR tube outside the sample[97,98] and they can be excluded from our anatomical discussions. In the modern spruce, the individual T_1 component around 800 ms is a mean value over the entire wood structure and it is associated with the three different T_2 components around 30, 5 and 0.9 ms (Fig. 4b). The most intense T_2 peak is around 30 ms (78%) and it can be attributed to free water in earlywood (EW) tracheids with a larger lumen size, in good agreement with previous works.[28,44,91,98] The small (7%) T_2 peak at around 5 ms is associated with free water in latewood (LW) tracheids, which are characterized by a smaller lumen size, in agreement with the literature.[28,44,91,98] The shortest T_2, instead, can be attributed to bound water in cell walls, which represent the 12% of the total water signal. The observation of three T_2 components and only one T_1 component indicates that exchange of water between the three sites (bound water as well as EW and LW free water) is fast in the T_1 time scale ($\tau_{ex} \ll$ 800 ms) but slow in the T_2 time scale ($\tau_{ex} \geq$ 1–30 ms). For the ancient spruce, two different T_1 peaks at around 1300 and 300 ms and five different T_2 peaks at around 400, 97, 18, 5 and 1.4 ms were observed. The T_1 component of 1300 ms (34%) can be associated with the T_2 component of 400 ms (52%), which can be attributed to water in large voids due to wood decay and empty resin channels (*i.e.*, full of water instead of resin), with a size of around 100 μm (as measured in the MR image of Fig. 1d). The shortest T_1 peak at around 300 ms, which is also the most intense (59%), can be associated with the four shorter T_2 peaks at around 97, 18, 5 and 1.4 ms. It should be noted that the peak at around 5 ms is not well-resolved and it is intermediate between the above-mentioned T_2 peaks at 18 and 1.4 ms, and this suggests a continuous distribution among these three different water populations. T_2 = 97 ms can be ascribed to water in large EW tracheid lumen (9%), T_2 = 18 ms can be ascribed to water in the rest of EW tracheid lumen (24%) and T_2 = 5 ms can be ascribed to LW tracheids (8%). Finally, T_2 = 1.4 ms arises from bound water in cell walls (7%). The free and bound water peaks are closer to each other than in the case of modern spruce due to the partial decay of the cell wall structure as well as related accelerated exchange between the two sites. In conclusion, both for the modern and the ancient wood samples, earlywood tracheids occupy a greater volume than latewood tracheids. The T_2 of the bound water in the ancient spruce wood is significantly longer than that in the modern spruce wood and there is a continuous distribution among the bound water, earlywood tracheids water and latewood tracheid water populations. This result denotes non-isolated water compartments and confirms the increase of the permeability of the cell wall due to its degradation,[13,99] as shown by the stretching of its T_2 component.

Chestnut

In Fig. 4c, the modern chestnut has only two T_1 components, while the ancient chestnut is characterized by four T_1 components. In Fig. 4d, the modern and the ancient chestnuts exhibit similar T_2 values. The ancient chestnut shows two high peaks at very long and very short T_2 values, and a greater compartmentalization of water

T_2 populations. Conversely, the modern chestnut has a major peak at an intermediate T_2 value and fewer water populations. The modern chestnut sample shows two T_1 components around 1800 and 500 ms, whereas it is characterized by four T_2 components around 175, 30, 5, and 0.4 ms. The T_1 = 1800 ms peak (46%) can be associated with T_2 = 175 and 30 ms peaks, which can be attributed to 11% of water in large vessels with a size of around 140–300 μm and to 18% of water in smaller pores with a size of around 60 μm, respectively. This agrees with the pore size measured on the respective MR image in Fig. 2a. The T_1 = 500 ms peak (54%), instead, can be associated with two T_2 components, 5 and 0.4 ms, that can be attributed, respectively, to water in fibres and parenchyma (55%), and to water in cell walls (16%). The three T_2 peaks associated with two sizes of vessels (around 140–300 and 60 μm) and with fibres and parenchyma show a continuous distribution, whereas the T_2 peak associated with cell walls is separated. The most intense T_2 peak is that associated with fibres and parenchyma (55%). The archaeological chestnut shows a greater compartmentalization of both T_1 and T_2 with four T_1 components around 3000, 900, 100 and 20 ms and six T_2 components of about 350, 78, 26, 10, 2 and 0.6 ms. T_1 = 3000 ms (11%) and T_2 = 350 ms (29%) can be interpreted as free water in very large vessels with a size of around 260–350 μm, being in good agreement with the fact that vessels with a size of around 260–350 μm are also the most abundant in the MR image of Fig. 2b. The second T_1 around 900 ms (6%) is associated with two different T_2 = 78 and 26 ms (5 and 3%) and these can be attributed to water in vessels with a size of 170 μm. The third T_1 peak at 100 ms (11%) is associated with the T_2 peak at around 10 ms (3%) and they can be attributed to water in vessels with a size of 80 μm. Moreover, there is a continuous distribution among the peaks with T_2 = 78, 26 and 10 ms that indicates the existence of not discrete relaxation populations in vessels. The last peak at very short T_1 of 20 ms (73%) can be associated with the two shortest T_2 peaks, at 2 and 0.6 ms (17 and 42%), and they are interpreted to arise from cell walls and fibers/parenchyma, respectively. Furthermore, the continuous distribution between the water population in fibres/parenchyma and that in cell walls suggests that there is water exchange between them. In conclusion, on average, the ancient chestnut shows a greater water compartmentalization and it is characterized by longer T_2 relaxation times compared to the modern chestnut but it has two T_1 components that are longer than those of the modern chestnut and two T_1 components that are shorter. The shortening of these two T_1 components is caused by the presence of paramagnetic inclusions, *i.e.*, iron-tanning substances,[28,99] in fibres, parenchyma, and cell walls. A strong degradation process of the wood cell wall, which has increased its water permeability and porosity, was observed, in good agreement with our previous work.[28]

Maple

In Fig. 4e, the modern maple is characterized by only one T_1 peak, whereas the ancient maple is characterized by three T_1 peaks. In Fig. 4f, the modern and the ancient maple samples have a quite similar T_2 distribution. However, the ancient maple shows an additional T_2 component on the long side. The only one T_1 component of the modern maple, around 1600 ms, can be considered a mean value over the overall structure. This T_1 is associated with three different T_2 at around 70, 15, and 1.5 ms that can be attributed, respectively, to water in vessels (44%) with a mean size of 36 ± 8 μm (measured on the MR image of Fig. 3a), water in fibres and parenchyma (50%), and water in cell walls (6%). There is a marked continuous distribution between the T_2 peaks of vessels and fibres and the most intense peak is associated with fibres, which represent the 50% of the wood. For the ancient maple sample, the T_1 component around 2100 ms and the T_2 component around 350 ms indicate water in larger vessels (around 86 ± 10 μm, measured on the MR image in Fig. 3d).[97,98] The second T_1 = 700 ms can be associated with the two T_2 = 78 and 16 ms and they are the characteristic, respectively, of water in smaller vessels (around 40 ± 4 μm, measured on the MR image in Fig. 3d) and water in fibres and parenchyma (67%), respectively. Here, a continuous distribution among vessels, fibres, and parenchyma can be observed. The last T_1 = 200 ms is associated with the last T_2 = 2.3 ms and they can be attributed to cell walls (4%). For the modern sample, also in the ancient sample, fibres are the most abundant element and constitute 67% of the wood.

In conclusion, there is a greater compartmentalization of T_1 in the ancient maple compared to the modern one. This may indicate possible structural changes in the ancient maple induced by a decay process. These changes are confirmed by the increase of T_2 associated with the cell walls and the larger size of vessels in the ancient sample compared to the modern sample. However, it is worth noting that, while the specimen comes from the tree trunk for the ancient maple, the specimen was collected from a branch for the modern maple and this may be the reason of some structural differences observed in the two specimens.

Diffusion

Diffusion of water in the wood samples was measured in the tangential direction. Because in the diffusion experiments, magnetization remained in the transverse plane altogether for 10 ms before detection, and the bound water signal was filtered out due to its short T_2. Altogether, three diffusion decay components were observed for all samples. However, for one of the components, the observed apparent diffusion coefficient value did not change when the observation time was increased, indicating non-restricted diffusion. Therefore, this component was interpreted to arise from bulk water on sample surfaces. For the two other diffusion components, the apparent diffusion coefficient values (D) as a function of the observation time (Δ) obtained from ILT analysis are shown in Fig. 5–7. The diffusion coefficients decrease with the increasing observation time due to restricted diffusion. The resulting surface-to-volume ratio (S/V) obtained from eqn (1) and the pore diameter (d), calculated from S/V, with the ratio between the weights ($p_1 : p_2$) of the two d components are reported in Table 4, along with the average tortuosity (τ) obtained respectively from eqn (2) for spruce samples and from eqn (3) for chestnut and maple samples.

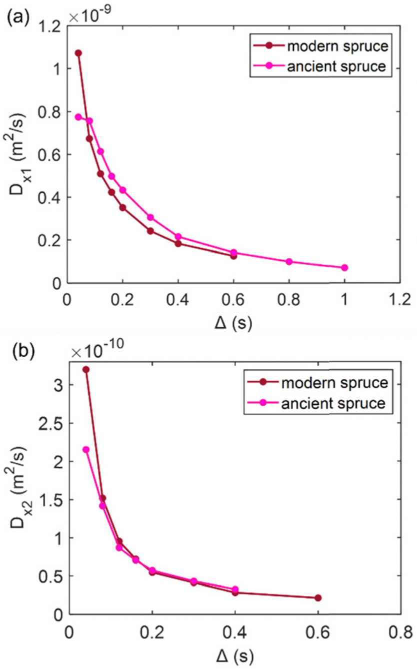

Fig. 5 (a) The first component (D_{x1}) and (b) the second component (D_{x2}) of the diffusion coefficient (D) measured along the x-axis (perpendicular to the wood grain) as a function of the observation time (Δ) and calculated using the ILT method[76] for modern and ancient spruce samples. The intensity ratio between D_{x1} and D_{x2} components is 1 : 0.10 and 1 : 0.26 for the modern spruce and the ancient spruce, respectively.

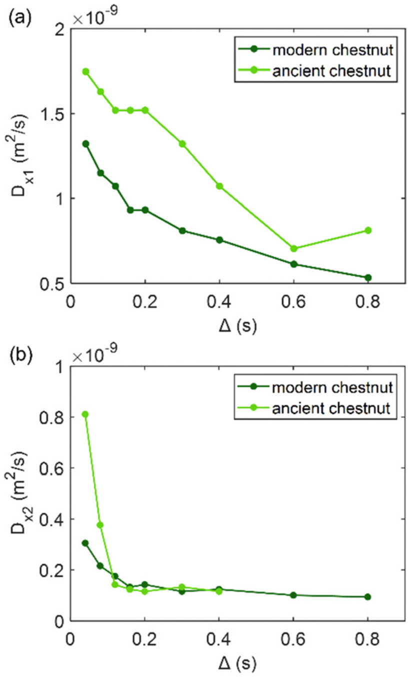

Fig. 6 (a) The first component (D_{x1}) and (b) the second component (D_{x2}) of the diffusion coefficient (D) measured along the x-axis (perpendicular to the wood grain) as a function of the observation time (Δ) and calculated using the ILT method[76] for modern and ancient chestnut samples. The intensity ration ratio between D_{x1} and D_{x2} components is 1 : 0.30 and 1 : 0.47 for the modern chestnut and the ancient chestnut, respectively.

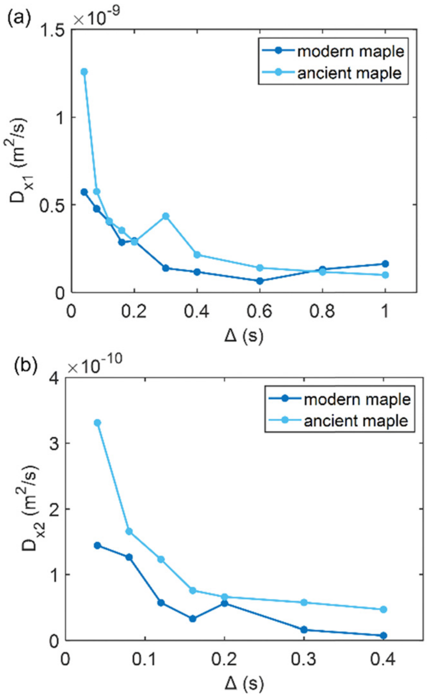

Fig. 7 (a) The first component (D_{x1}) and (b) the second component (D_{x2}) of the diffusion coefficient (D) measured along the x-axis (perpendicular to the wood grain) as function of the observation time (Δ) and calculated using the ILT method[76] for modern and ancient maple samples. The intensity ratio between D_{x1} and D_{x2} components is 1 : 0.38 and 1 : 0.06 for the modern maple and the ancient maple, respectively.

It is worth noting that the major weakness of NMR diffusion is that the maximum length scale covered by this technique (on the order of $\ell_D = \sqrt{2D_0\Delta}$, where $D_0 = 2.2 \times 10^{-9}$ m^2 s^{-1} is the bulk water diffusion coefficient) is intrinsically limited by the characteristic T_1 of the wood material, which limits the maximum diffusion delay ($\Delta < T_1$).

The results obtained from diffusion analyses are discussed separately for spruce, chestnut and maple in the following sections.

Spruce

In Fig. 5, the water diffusion measured perpendicular to the wood grain is quite similar both in the modern and in the ancient spruce samples. The two diffusion components, D_{x1} and D_{x2}, are associated with water inside pores of sizes d_1 = 31.7 ± 1.6 μm and d_2 = 24.4 ± 2.8 μm in the modern spruce and with pores of sizes d_1 = 35.7 ± 1.8 μm and d_2 = 24.2 ± 2.9 μm in the ancient spruce, respectively. The pore size d_1 can be attributed to the lumen size of earlywood tracheids, whereas the pore size d_2 can be attributed to the lumen size of latewood tracheids, in good agreement with results reported in the literature.[100] Both D_{x1} and d_1 are a bit higher in the ancient spruce indicating that their earlywood tracheids have a bit larger lumen size than those of the modern spruce. The relative intensity of the earlywood component was about 10 times higher than that of the latewood component, being in good

Table 4 Surface-to-volume ratio (S/V) obtained from eqn (1), pore diameter (d) calculated from S/V together with the ratio between the weights of the two d components ($p_1:p_2$), and mean tortuosity (τ) calculated as the weighted average between the tortuosity obtained for the two diffusion populations from eqn (2) for spruce samples and from eqn (3) for chestnut and maple samples

	$\left(\frac{S}{V}\right)_1$ (m^{-1})	$\left(\frac{S}{V}\right)_2$ (m^{-1})	d_1 (μm)	d_2 (μm)	$p_1:p_2$	τ
Modern spruce	$(1.9 \pm 0.1) \times 10^5$	$(2.5 \pm 0.3) \times 10^5$	31.7 ± 1.6	24.4 ± 2.8	1 : 0.10	16.9 ± 1.1
Ancient spruce	$(1.7 \pm 0.1) \times 10^5$	$(2.5 \pm 0.3) \times 10^5$	35.7 ± 1.8	24.2 ± 2.9	1 : 0.26	23.3 ± 1.3
Modern chestnut	$(1.3 \pm 0.1) \times 10^5$	$(2.4 \pm 0.3) \times 10^5$	45.2 ± 2.9	25.1 ± 3.0	1 : 0.30	7.2 ± 2.0
Ancient chestnut	$(7.4 \pm 0.4) \times 10^4$	$(2.3 \pm 0.1) \times 10^5$	81.5 ± 4.5	26.5 ± 1.6	1 : 0.47	23.9 ± 0.2
Modern maple	$(2.1 \pm 0.2) \times 10^5$	$(2.5 \pm 0.3) \times 10^5$	28.1 ± 2.9	23.7 ± 3.0	1 : 0.38	65.2 ± 0.7
Ancient maple	$(1.9 \pm 0.1) \times 10^5$	$(2.4 \pm 0.3) \times 10^5$	30.8 ± 1.5	24.6 ± 2.8	1 : 0.06	87.5 ± 0.6

agreement with the relaxation experiments. The mean tortuosity is higher in the ancient spruce (τ = 23.3 ± 1.3) than in the modern spruce (τ = 16.9 ± 1.1). This result suggests that on average water motion in the archaeological sample is more tangled than in the modern sample.

Chestnut

Fig. 6 shows that on average the first component D_{x1} of the diffusion coefficient in the archaeological chestnut is higher than that in the modern chestnut. Conversely, the component D_{x2} is similar in both samples. The two derived pore sizes d_1 and d_2 can be associated with small vessels and with fibers and parenchyma, respectively. For the ancient chestnut, d_1 = 81.5 ± 4.5 μm, whereas for the modern chestnut d_1 = 45.2 ± 2.9 μm. This result indicates that vessels are smaller in the modern chestnut compared to the ancient one. Indeed, this pore size can be attributed to the smallest size of vessels that were measured on the μ-MR image for both wood samples (Fig. 2a and d). μ-MRI showed that the smallest size of vessels in the ancient chestnut (~80 μm) was larger than that in the modern chestnut (~60 μm). The pore size d_2 = 26.5 ± 1.6 for the ancient chestnut and d_2 = 25.1 ± 3.0 for the modern chestnut suggests that fibres and parenchyma have a similar size in both wood samples. The mean tortuosity is three times greater in the archaeological sample (τ = 23.9 ± 0.2) than that in the modern sample (τ = 7.2 ± 2.0) indicating that water motion is less easy in the archaeological sample. This result can be explained considering the high content of inclusions (*i.e.* iron-tanning substances[28,99]) stored in the structure of the ancient wood, as observed in the MR images (Fig. 2d–f). The inclusions lead to the formation of new compartments and water pools that make the ancient wood structure more complex.

Maple

Fig. 7 shows that the two diffusion components, D_{x1} and D_{x2}, are quite similar in the modern maple and ancient maple. These two water diffusion components are associated with two different pore sizes, d_1 and d_2, that are = 28.1 ± 2.9 and 23.7 ± 3.0 μm for the modern maple and 30.8 ± 1.5 and 24.6 ± 2.8 μm for the ancient maple, respectively. The intrinsic limitation due to the T_1 only allowed us to probe water diffusion in small vessels (quantified by the diameter d_1) of the ancient maple but not in the large vessels (with a size of around 86 μm) measured instead on the MR image (Fig. 3d). From diffusion, both the vessels size (d_1) and the size of fibres and parenchyma (d_2) are quite similar for both the ancient and modern samples. Moreover, it seems that vessels and fibers have a similar size in the modern sample. However, the mean tortuosity is greater in the ancient maple (τ = 87.5 ± 0.6) than that in the modern one (τ = 65.2 ± 0.7). This result suggests that on average water moves hardly in the archaeological wood.

Cryoporometry

T_2 relaxation distributions and signal intensities are both plotted *versus* temperature for ancient and modern spruce, chestnut, and maple in Fig. 8–10, respectively. Moreover, as an example, the T_2 distribution at two different temperatures, one above (T = 278 K) and one below (T = 269 K), and a melting point of 273 K are reported. Different signal contributions were separated, such as earlywood (EW), latewood (LW), micropore (MP) and bound water (BW). The two components observed below 273 K can be associated with two populations of bound water in the cell wall: BW has the shorter T_2 and arises from water molecules hydrogen bonded to the hydroxyl groups and between the cellulose chains, whereas MP water has the longer T_2 component and originates from water in cell wall micropores.[48,101] It can be seen that, in all modern samples, the bound water signal intensity decreases after the bulk melting point, most probably because the bound water and free water signals are partially mixed due to molecular exchange.[48,102] We note that the exchange cannot take place below the bulk melting point, as free water is frozen. A similar trend was not observed in the ancient counterparts, suggesting differences in the structure and dynamics. Furthermore, in all cases, water associated with tracheid/vessel lumens is frozen, as no clear signal is observed corresponding to those at lower temperatures, and as these structures are bigger in nature, the main melting point of these structures coincides with the bulk melting point of water (T = 273 K). In all the modern wood samples, the EW and LW signals constitute most of the full signal, while in the ancient counterparts, the relative amount of EW and LW water is significantly smaller, and other components (*i.e.*, cell walls) also play crucial role in the total signal, in good agreement with relaxometry results showing an increased T_2 peak associated with water in cell walls. All ancient wood samples have MP water signals greater than that of their modern counterparts, indicating an increase of the micropore water content in the ancient wood samples.

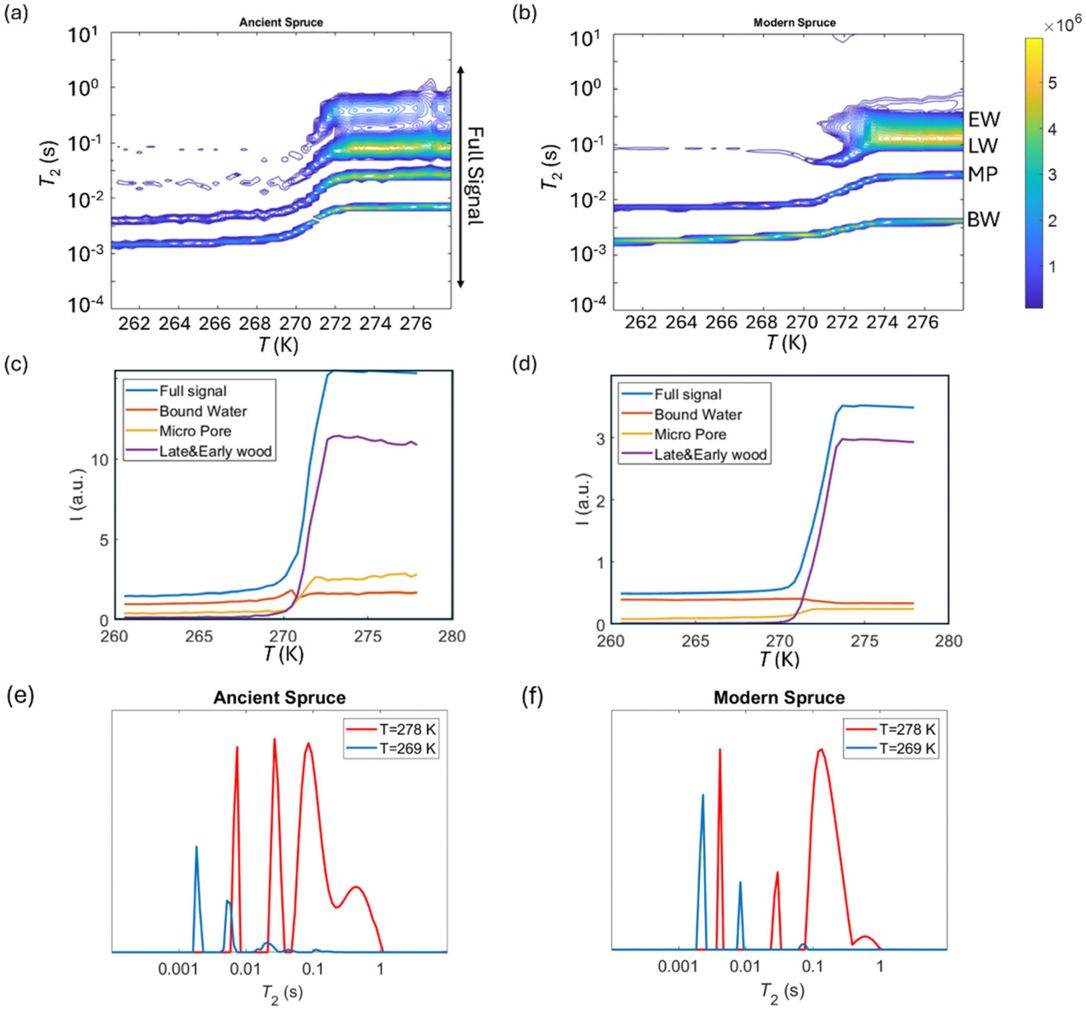

Fig. 8 T_2 relaxation distributions *versus* temperature for ancient spruce (a) and modern spruce (b). EW, LW, MP, and BW refer to earlywood, latewood, micropore and bound water signals, respectively. The signal intensity of each component *versus* temperature for ancient spruce (c) and modern spruce (d) and the full signal region indicated in (a). T_2 distributions for ancient spruce (e) and modern spruce (f) before and after the melting point (T = 273 K).

This result confirms the degradation suffered by the cell wall, corresponding to an increased permeability, which was already detected by relaxometry, diffusometry and microimaging. In the case of the ancient chestnut, also an extra signal is present (Fig. 9a), behaving similarly as the LW and EW signals, which is therefore likely attributed to similar bigger pore structures (*i.e.*, vessels) associated with the wood structure. This is in agreement with the increased compartmentalization of vessels in the ancient chestnut, characterized by three main relaxation components belonging to three different vessel sizes of around 260–350 μm, 170 μm and 80 μm detected from relaxation measurements and observed in μ-MR images.

The relative amounts of water in pores with a size of below 8 nm, corresponding to the ratio of the signal intensities measured at 265 K and above 273 K, are shown in Fig. 11. The main result is that in all ancient wood samples it is smaller than in modern wood samples. The decrease of water portion in small pores corresponds to the decreased amount of bound water in the archaeological wood samples due to decay of cell wall structures.[30,103–105]

Overall porosity

The combination of μ-MRI, relaxometry, diffusometry, and cryoporometry allowed us to cover several dimensional scales of wood samples, from cell wall cavities to sub-millimeter pores. In the following sections, we summarize the characteristics of the overall porosity and the different water distributions in each species of wood obtained by combining all the NMR techniques and we explain how these characteristics change as a result of the decay process.

Spruce

Both the modern spruce and the ancient spruce are characterized by at least three water populations corresponding to three different pore sizes: earlywood tracheids, latewood tracheids and cell walls. In addition, the ancient spruce also shows a fourth population of water in the resin canals with a size of

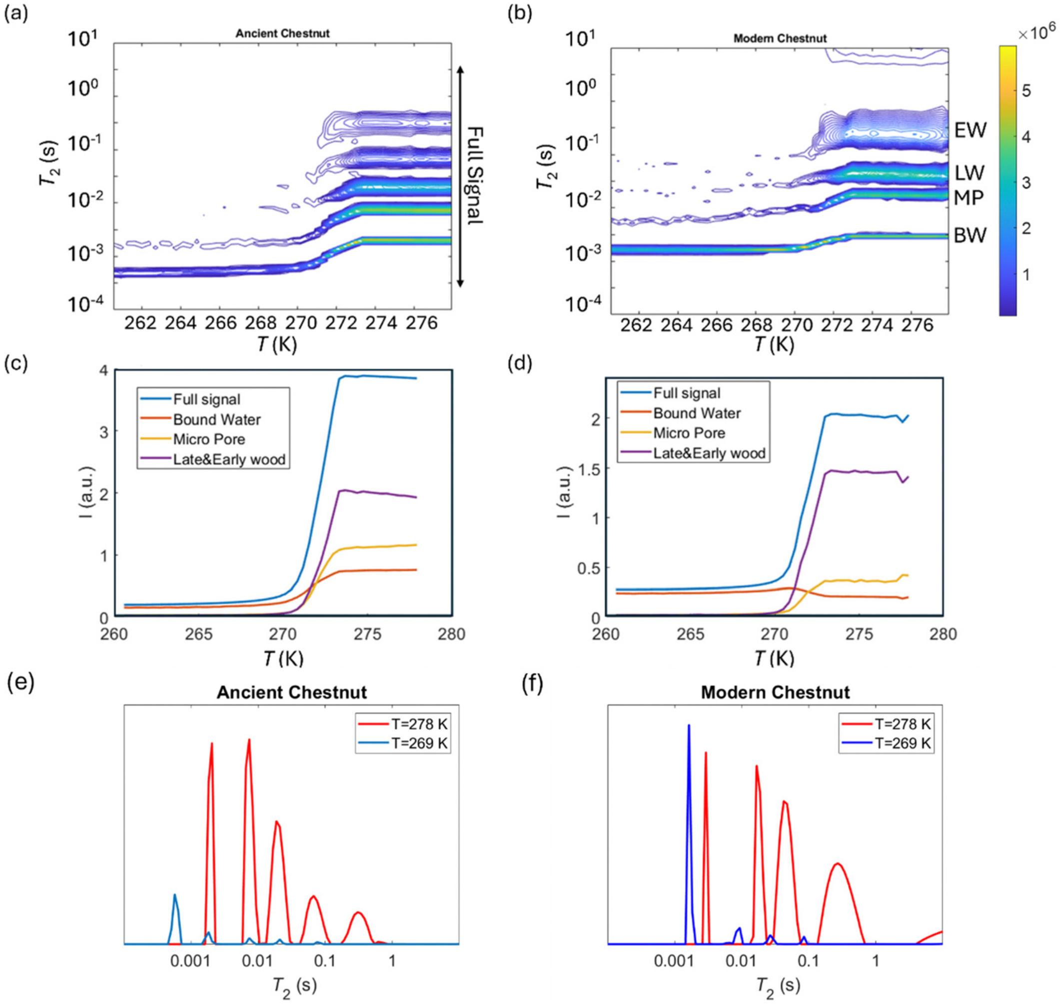

Fig. 9 T_2 relaxation distributions *versus* temperature for the ancient chestnut (a) and the modern chestnut (b). EW, LW, MP, and BW refer to earlywood, latewood, micropore and bound water signals, respectively. The signal intensity of each component *versus* temperature for the ancient chestnut (c) and the modern chestnut (d) and the full signal region indicated in (a). T_2 distributions for the ancient chestnut (e) and the modern chestnut (f) before and after the melting point (T = 273 K).

around 100 μm, which was not seen for the modern spruce where the resin canals, having a size of about 75 μm, are still full of resin rather than water. The earlywood tracheids in the ancient spruce have a larger diameter (~36 μm) than in the modern spruce (~32 μm). The similar T_1 and T_2 values along with the close diffusion coefficient (D_{x2}) and pore size (d_2) indicate that LW tracheids have similar sizes in both the modern spruce and the ancient spruce. The increase of T_2 associated with water in cell walls and the decrease of the water amount in pores smaller than 8 nm indicate that the cell walls of the archaeological wood can retain less bound water. This is most probably due to the decay of the cell walls, and it may be possible that bigger pores appeared in the cell walls of the ancient wood samples. The decay process of the wood cell wall was also observed in the MR images in Fig. 1 and in the optical microscopy images reported in our previous work.[28] Moreover, the non-isolated water compartments in EW tracheids, LW tracheids and cell walls, along with the increased signal of MP water, confirm the increase of the cell wall permeability due to its degradation. The higher tortuosity measured for the ancient spruce is in agreement with the greater number of components of the relaxation times T_1 and T_2 indicating the increase of water compartmentalization in the structure of the archaeological wood. This increased compartmentalization is due to the presence of inclusions, spores, and residues of fungal hyphae,[28] and to the overall structural decay that led to the formation of new pores and water pools.

Chestnut

The modern and the ancient chestnut belong to the hardwood group that is characterized by structures with different sizes that correspond to several water populations. The modern chestnut has three mean vessel sizes of around 300, 140, and 60 μm, whereas the ancient chestnut has four vessels sizes of about 350, 260, 170, and 80 μm. In the ancient chestnut, the vessels with sizes in the range of 260–350 μm are the most abundant. On average, the ancient chestnut is characterized by larger vessels compared to the modern chestnut and it shows a

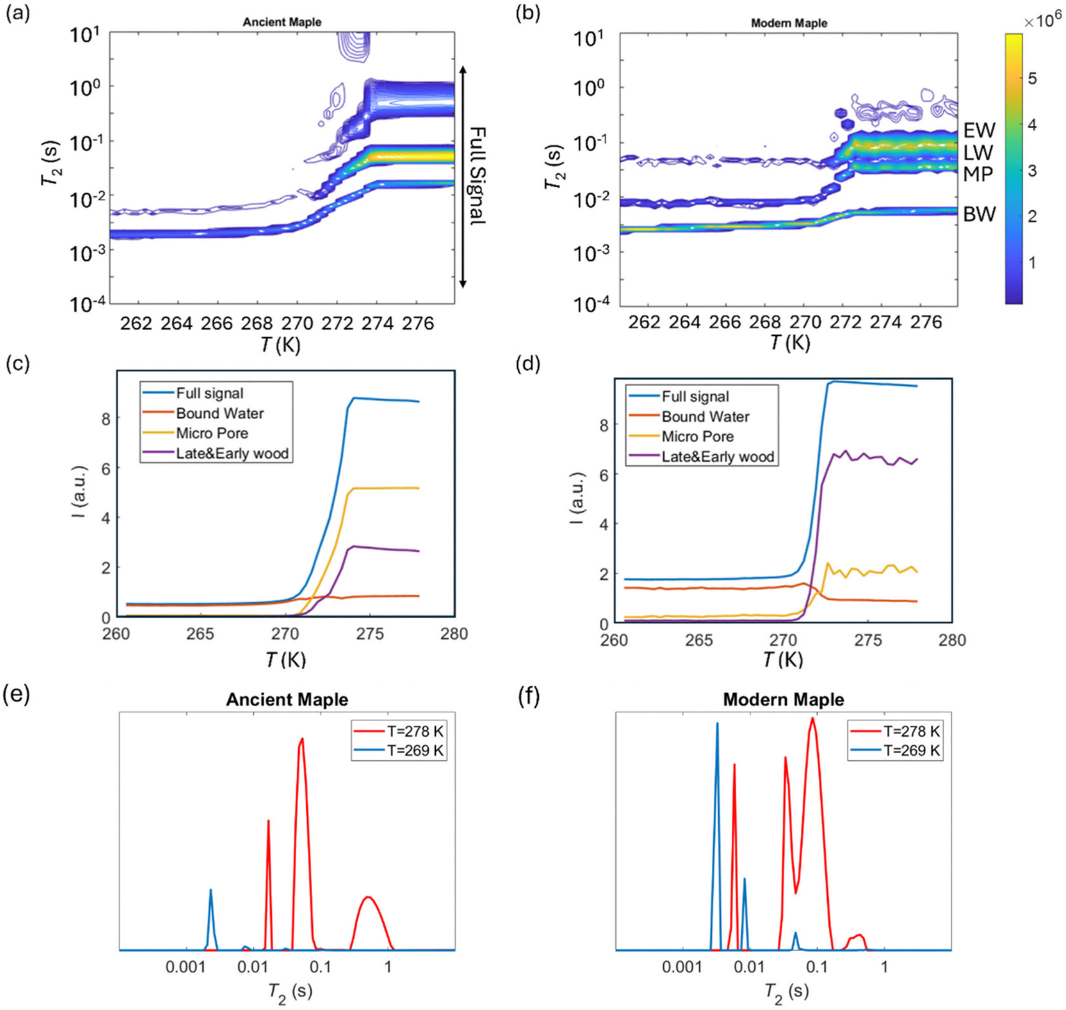

Fig. 10 T_2 relaxation distributions *versus* temperature for the ancient maple (a) and the modern maple (b). EW, LW, MP, and BW refer to earlywood, latewood, micropore and bound water signals, respectively. The signal intensity of each component *versus* temperature for the ancient maple (c) and the modern maple (d) and the full signal region indicated in (a). T_2 distributions for the ancient maple (e) and the modern maple (f) before and after the melting point (T = 273 K).

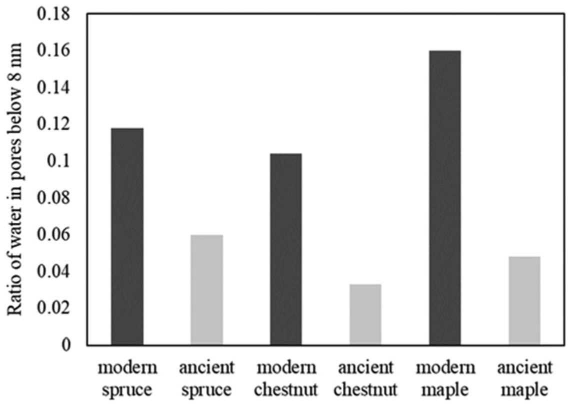

Fig. 11 The amount of water in pores with a diameter of below 8 nm, corresponding to the ratio of the signal intensities measured at 265 K and above 273 K.

greater water compartmentalization, as indicated by its greater number of T_1 and T_2 components and by its higher mean tortuosity. The shortening of the T_1 components in the ancient chestnut is caused by the significant presence of paramagnetic inclusions, *i.e.*, iron-tanning substances,[28,99] in fibres, parenchyma and cell walls. Paramagnetic inclusions, that totally or partially obstruct vessels in the ancient sample, are also responsible for the formation of new compartments throughout the wood structure. Moreover, it is worth noting that, in the ancient wood, the T_2 associated with water in vessels of size = 80 μm and with fibers/parenchyma is shorter than the T_2 associated with water in vessels of size = 60 μm and fibers/parenchyma in the modern wood. This indicates that also the T_2 may be shortened by the effect of paramagnetic substances. The decrease of the bound water amount in small pores (<8 nm) of the cell wall and the increased intensity of the MP water signal and of the T_1 and T_2 peaks associated with water in the cell walls of the ancient chestnut suggest a strong degradation process of the wood cell wall, which shows higher permeability and porosity, in good agreement with our previous work.[28]

Maple

Three different water populations, corresponding to vessels, fibres and parenchyma, were detected for both the modern maple and the ancient maple. The modern maple is characterized by only one size of vessels, around 36 μm, whereas the ancient maple is characterized by two sizes, around 86 and 40 μm. Water is mostly stored in fibres and parenchyma, with a similar mean size of 25 μm in both the modern maple and the ancient maple. The similar size of fibres and parenchyma in both the wood samples is also confirmed by their close T_2 values. The increase of T_2 of water stored in cell walls in the archaeological maple suggests the increase of their size. Moreover, the decrease of the water content in pores below 8 nm of the cell walls along with the increase of the MP water signal in the ancient maple suggest a greater permeability of the cell walls. Again, the tortuosity is higher in the archaeological sample than in the modern sample, implying a more complex structure in the ancient wood. Indeed, the higher number of T_1 and T_2 components in the ancient sample indicates its greater structural compartmentalization that is induced by the decay process and the presence of spores and residues of fungal hyphae.[28] However, the aforementioned results must be taken with care because the specimen comes from the tree trunk for the ancient maple and the specimen was collected from a branch for the modern maple. It may be that the total porosity and anatomical structures in the modern maple are not yet well developed compared to those in the ancient maple, due to their different growth stages.

Conclusions

Research in the field of conservation sciences is constantly engaged in the search for innovative non-destructive techniques for the investigation of archaeological submerged wood. Ideal alternative techniques should allow obtaining information complementary or similar to that provided by conventional optical microscopy. This requirement has led to the advancement of the micro-imaging NMR technique with the optimization of its resolution such that it can resolve anatomical elements of wood with minimum dimensions around 10 micrometers. Additionally, wood anatomical features and water dynamics can also be characterized indirectly using techniques such as NMR relaxometry, NMR diffusometry, and NMR cryoporometry, which provide the characterization of both static and dynamic systems, *e.g.*, MR imaging *vs.* diffusion-weighted imaging (DWI). Specifically, NMR cryoporometry overcomes the resolution limit of MRI and diffusion and the paramagnetic bias of relaxometry, allowing us to go below 10 microns and investigate wood structures on the nanometric scale (*i.e.*, cell walls). Combining the above-mentioned NMR techniques and using appropriate mathematical models, it was possible to implement an innovative NMR protocol to obtain a comprehensive analysis of the porous wood structure. This work laid the foundation for the application of the new NMR protocol to the archaeological waterlogged wood. The multi-modal approach allowed us to detect the incipient cell wall decay, the accumulation of inclusions (black areas in MR images) and the biological infestations in the three archaeological wood samples studied in this work. Decay, inclusions, fungal spores, and hyphae have increased the structural complexity (corresponding to a higher tortuosity) of the ancient wood with the formation of new populations of water, identified by new T_1 and T_2 components, compared to the modern wood samples. All three ancient wood samples are characterized by a lower amount of water inside pores with a size of below 8 nm compared to the modern wood samples, indicating that the cell walls in the ancient wood hold more water in bigger pores and increase their permeability. To the best of our knowledge, this is the first study to jointly apply four different NMR techniques to encompass all the relevant length scales of wood. In future work, the protocol needs to be tested on a higher number of samples to verify its validity on several wood species. It would be preferable to develop two separate protocols, one for the characterization of softwood and the other for hardwood. Wood samples can have quite different structures depending on the individual, the age of the wood, and the location of the sample in the trunk/branch. Therefore, the differences between modern and ancient wood samples will require careful evaluation and correct interpretation.

Data availability

Data for this article are available at "STAGNO 2024" at 10.6084/m9.figshare.26196911.

Conflicts of interest

There are no conflicts to declare.

Acknowledgements

V. Stagno acknowledges the funding of Lazio Region under the Torno Subito 2018 program of the Department of Education, Research, School, University, and the Regional Body for the Right to Study and Knowledge (DiSCo). O. Mankinen acknowledges the Research Council of Finland (grant number 355001), KAUTE foundation and Finnish Cultural Foundation-Kalle and Dagmar Välimaan Fund. V.-V. Telkki acknowledges European Research Council (grant number 772110), the Research Council of Finland (grant number 340099) and Kvantum institute (University of Oulu) for financial support. Part of this work was carried out with the support of the Centre for Material Analysis, the University of Oulu, Finland. The authors thank the national Italian agreement between CRUI-CARE and Royal Society of Chemistry (RSC) for funding the article processing charge (APC).

Notes and references

1 W. H. Schoch, G. Bigga, U. Böhner, P. Richter and T. Terberger, New insights on the wooden weapons from

the Paleolithic site of Schöningen, *J. Hum. Evol.*, 2015, **89**, 214–225.

2 C. G. Björdal, T. Nilsson and G. Daniel, Microbial decay of waterlogged archaeological wood found in Sweden. Applicable to archaeology and conservation, *Int. Biodeterior. Biodegrad.*, 1999, **43**, 63–73.

3 N. B. Pedersen, J. J. Łucejko, F. Modugno and C. Björdal, Correlation between bacterial decay and chemical changes in waterlogged archaeological wood analysed by light microscopy and Py-GC/MS, *Holzforschung*, 2021, **75**, 635–645.

4 N. B. Pedersen, C. G. Björdal, P. Jensen and C. Felby, in *Stability of Complex Carbohydrate Structures: Biofuels, Foods, Vaccines and Shipwrecks*, ed. S. E. Harding, The Royal Society of Chemistry, 2012, pp. 160–187.

5 R. A. Blanchette, A review of microbial deterioration found in archaeological wood from different environments, *Int. Biodeterior. Biodegrad.*, 2000, **46**, 189–204.

6 C. Gjelstrup Björdal, Microbial degradation of waterlogged archaeological wood, *J. Cult. Herit.*, 2012, **13**, S118–S122.

7 K. E. High and K. E. H. Penkman, A review of analytical methods for assessing preservation in waterlogged archaeological wood and their application in practice, *Heritage Sci.*, 2020, **8**, 83.

8 Å. Henrik-Klemens, F. Bengtsson and C. G. Björdal, Raman Spectroscopic Investigation of Iron-Tannin Precipitates in Waterlogged Archaeological Oak, *Stud. Conserv.*, 2022, **67**, 237–247.

9 D. Cole Hamilton, B. Kaye, J. A. Chudek and G. Hunter, Nuclear magnetic resonance imaging of waterlogged wood, *Stud. Conserv.*, 1995, **40**, 41–50.

10 D. J. Cole-Hamilton, J. A. Chudek, G. Hunter and C. J. M. Martin, N.M.R. imaging of water in wood including waterlogged archaeological artefacts, *J. Inst. Wood Sci.*, 1990, **12**, 111–113.

11 J. I. Hedges, *The Chemistry of Archaeological Wood*, 1989.

12 R. Brunning and J. Watson, *Waterlogged wood Guidelines on the recording, sampling, conservation and curation of waterlogged wood*, English Heritage, 2010.

13 N. Macchioni, *Encyclopedia of Global Archaeology*, 2020.

14 M. Broda and C. A. S. Hill, Conservation of waterlogged wood—past, present and future perspectives, *Forests*, 2021, **12**, 1193.

15 M. N. Mortensen, H. Egsgaard, S. Hvilsted, Y. Shashoua and J. Glastrup, Characterisation of the polyethylene glycol impregnation of the Swedish warship Vasa and one of the Danish Skuldelev Viking ships, *J. Archaeol. Sci.*, 2007, **34**, 1211–1218.

16 *Conservation of cultural heritage. Guidelines for the management of waterlogged wood on archaeological terrestrial sites*, Europe, 2016.

17 M. Bardet, G. Gerbaud, Q. K. Trân and S. Hediger, Study of interactions between polyethylene glycol and archaeological wood components by 13C high-resolution solid-state CP-MAS NMR, *J. Archaeol. Sci.*, 2007, **34**, 1670–1676.

18 J. Stelzner, I. Stelzner, J. Martinez-Garcia, D. Gwerder, M. Wittköpper, W. Muskalla, A. Cramer, G. Heinz, M. Egg and P. Schuetz, Stabilisation of waterlogged archaeological wood: the application of structured-light 3D scanning and micro computed tomography for analysing dimensional changes, *Heritage Sci.*, 2022, **10**, 60.

19 Z. Walsh, E. R. Janeček, M. Jones and O. A. Scherman, Natural polymers as alternative consolidants for the preservation of waterlogged archaeological wood, *Stud. Conserv.*, 2017, **62**, 173–183.

20 V. Stagno, C. Moricca, L. Sadori, E. Dell'Aglio, R. Reale and S. Capuani, Evaluation of the efficacy of micro-Magnetic Resonance Imaging compared with light microscopy to investigate the anatomy of modern and ancient waterlogged wood, *Magn. Reson. Imaging*, 2023, **102**, 164–178.

21 J. L. Silva, C. S. Barata and J. Pissarra, Limitations and Obstacles on Wood Identification From Sculptures - Analysis of A Set of Gilded and Polychromed Flemish Artworks From The 15thCentury, *Int. J. Conserv. Sci.*, 2021, **12**, 349–360.

22 R. Bruzzone and M. C. Galassi, *Studying old master paintings: technology and practice: the National Gallery Technical Bulletin 30th anniversary conference postprints*, 2011, pp. 253–259.

23 K. Čufar, A. Balzano, L. Krže and M. Merela, Wood identification using non-destructive confocal laser scanning microscopy, *Les/Wood*, 2019, **68**, 19–29.

24 F. Ruffinatto, N. Macchioni, G. Boetto, P. Baas and R. Zanuttini, Reflected light microscopy as a non-invasive identification tool for wooden artefacts, *IAWA J.*, 2010, **31**, 317–331.

25 F. Ruffinatto, C. Cremonini, N. Macchioni and R. Zanuttini, Application of reflected light microscopy for non-invasive wood identification of marquetry furniture and small wood carvings, *J. Cult. Herit.*, 2014, **15**, 614–620.

26 S. Capuani, V. Stagno, M. Missori, L. Sadori and S. Longo, High-resolution multiparametric MRI of contemporary and waterlogged archaeological wood, *Magn. Reson. Chem.*, 2020, **58**, 860–869.

27 S. Longo, F. Egizi, V. Stagno, M. G. Di Trani, G. Marchelletta, T. Gili, E. Fazio, G. Favero and S. Capuani, A Multi-Parametric Investigation on Waterlogged Wood Using a Magnetic Resonance Imaging Clinical Scanner, *Forests*, 2023, **14**, 276.

28 V. Stagno, S. Mailhiot, S. Capuani, G. Galotta and V. V. Telkki, Testing 1D and 2D single-sided NMR on Roman age waterlogged woods, *J. Cult. Herit.*, 2021, **50**, 95–105.

29 C. Moricca, V. Stagno, N. M. Hamza, G. Favero, L. Sadori and S. Capuani, The High Potential of Micro-Magnetic Resonance Imaging for the Identification of Archaeological Reeds: The Case Study of Tutankhamun, *Heritage*, 2023, **6**, 7170–7180.

30 J. Guo, L. Xiao, L. Han, H. Wu, T. Yang, S. Wu, Y. Yin and L. A. Donaldson, Deterioration of the cell wall in waterlogged wooden archeological artifacts, 2400 years old, *IAWA J.*, 2019, **40**, 820–844.

31 J. Kowalczuk, A. Rachocki, M. Broda, B. Mazela, G. A. Ormondroyd and J. Tritt-Goc, Conservation process of

archaeological waterlogged wood studied by spectroscopy and gradient NMR methods, *Wood Sci. Technol.*, 2019, **53**, 1207–1222.

32 P. M. Kekkonen, V. V. Telkki and J. Jokisaari, Determining the highly anisotropic cell structures of Pinus sylvestris in three orthogonal directions by PGSTE NMR of absorbed water and methane, *J. Phys. Chem. B*, 2009, **113**, 1080.

33 Ö. Gezici-Koç, S. J. F. Erich, H. P. Huinink, L. G. J. van der Ven and O. C. G. Adan, Bound and free water distribution in wood during water uptake and drying as measured by 1D magnetic resonance imaging, *Cellulose*, 2017, **24**, 535–553.

34 P. T. Callaghan, *Principle of Nuclear Magnetic Resonance Microscopy*, 1994.

35 D. Shaw, *Fourier transform NMR spectroscopy*, Elsevier Scientific Pub Co, 1976.

36 C. L. Partain, *Nuclear Magnetic Resonance NMR Imaging*, Saunders College Publishing, 1983.

37 C. L. Maini, G. Valle, M. G. Bonetti and M. A. Macrì, *Principi di tomografia a risonanza magnetica nucleare*, I.S.U. Università Cattolica Milano, 1987.

38 E. L. Hahn, An accurate nuclear magnetic resonance method for measuring spin-lattice relaxation times, *Phys. Rev.*, 1949, **76**, 145.

39 J. Keeler, *Understanding NMR Spectroscopy*, 2nd edn, Wiley, 2010.

40 U. Mikac, M. Merela, P. Oven, A. Sepe and I. Serša, Mr study of water distribution in a beech (Fagus sylvatica) branch using relaxometry methods, *Molecules*, 2021, **26**, 4305.

41 R. E. Hernández and C. B. Cáceres, Magnetic resonance microimaging of liquid water distribution in sugar maple wood below fiber saturation point, *Wood Fiber Sci.*, 2010, **42**, 259–272.

42 C. Cai, M. A. Javed, S. Komulainen, V. V. Telkki, A. Haapala and H. Heräjärvi, Effect of natural weathering on water absorption and pore size distribution in thermally modified wood determined by nuclear magnetic resonance, *Cellulose*, 2020, **27**, 4235–4247.

43 S. Hiltunen, A. Mankinen, M. A. Javed, S. Ahola, M. Venäläinen and V. V. Telkki, Characterization of the decay process of Scots pine caused by Coniophora puteana using NMR and MRI, *Holzforschung*, 2020, **74**, 1021–1032.

44 V. V. Telkki, Wood characterization by NMR & MRI of fluids, *eMagRes*, 2012, **1**, 1.

45 G. Costantini, S. Capuani, F. A. Farrelly and A. Taloni, A new perspective of molecular diffusion by nuclear magnetic resonance, *Sci. Rep.*, 2023, **13**, 1–19.

46 V. Stagno, F. Egizi, F. Corticelli, V. Morandi, F. Valle, G. Costantini, S. Longo and S. Capuani, Microstructural features assessment of different waterlogged wood species by NMR diffusion validated with complementary techniques, *Magn. Reson. Imaging*, 2021, **83**, 139–151.

47 V. Stagno and S. Capuani, Decay of a Roman age pine wood studied by micro magnetic resonance imaging, diffusion nuclear magnetic resonance and portable nuclear magnetic resonance, *Acta IMEKO*, 2022, **11**, 1–10.

48 P. M. Kekkonen, A. Ylisassi and V. V. Telkki, Absorption of water in thermally modified pine wood as studied by nuclear magnetic resonance, *J. Phys. Chem. C*, 2014, **118**, 2146–2153.

49 B. Blümich, M. Baias, C. Rehorn, V. Gabrielli, D. Jaschtschuk, C. Harrison, C. Invernizzi and M. Malagodi, Comparison of historical violins by non-destructive MRI depth profiling, *Microchem. J.*, 2020, **158**, 105219.

50 N. Proietti, D. Capitani and V. Di Tullio, Applications of nuclear magnetic resonance sensors to cultural heritage, *Sensors*, 2014, **14**(4), 6977–6997.

51 S. Viel, D. Capitani, N. Proietti, F. Ziarelli and A. L. Segre, NMR spectroscopy applied to the Cultural Heritage: A preliminary study on ancient wood characterisation, *Appl. Phys. A: Mater. Sci. Process.*, 2004, **79**, 357–361.

52 V. Di Tullio, D. Capitani, A. Atrei, F. Benetti, G. Perra, F. Presciutti, N. Proietti and N. Marchettini, Advanced NMR methodologies and micro-analytical techniques to investigate the stratigraphy and materials of 14th century Sienese wooden paintings, *Microchem. J.*, 2016, **125**, 208–218.

53 C. Casieri, L. Senni, M. Romagnoli, U. Santamaria and F. De Luca, Determination of moisture fraction in wood by mobile NMR device, *J. Magn. Reson.*, 2004, **171**(2), 364–372.

54 B. Blümich, L. Ciobanu and S. Haber-Pohlmeier, *Magnetic resonance microscopy: instrumentation and applications in engineering, life science and energy research*, John Wiley & Sons, Inc., Hoboken, NJ, 2022.

55 B. J. Balcom and M. Zhang, *Magn. Reson. Microsc.*, 2022, 337–353.

56 V. Di Donato, M. R. Ruello, V. Liuzza, V. Carsana, D. Giampaola, M. A. Di Vito, C. Morhange, A. Cinque and E. Russo Ermolli, Development and decline of the ancient harbor of Neapolis, *Geoarchaeology*, 2018, **33**, 542–557.

57 D. Giampaola, V. Carsena, G. Boetto, F. Crema, C. Florio, D. Panza, B. Pizzo, C. Capretti, G. Galotta, G. Giachi, N. Macchioni, M. P. Nugari and M. Bartolini, *Archaeol. maritima Mediterr. Int. J. Underwater Archaeol.*, 2005, **2**, 1–216.

58 E. A. Wheeler, InsideWood - A web resource for hardwood anatomy.

59 P. Baas, N. Blokhina, T. Fujii, P. E. Gasson, D. Grosser, I. Heinz, J. Ilic, J. Xiaomei, R. Miller, L. A. Newsom, S. Noshiro, H. G. Richter, M. Suzuki, T. Terrazas, E. Wheeler and A. Wiedenhoeft, IAWA List of microscopic features for softwood identification, *IAWA J.*, 2004, **25**, 1–70.

60 D. J. B. White, E. A. Wheeler, P. Baas and P. E. Gasson, IAWA List of Microscopic Features for Hardwood Identification by an IAWA Committee, *IAWA J.*, 1991, **10**, 219–332.

61 F. Ruffinatto, A. Crivellaro and A. C. Wiedenhoeft, Review of macroscopic features for hardwood and softwood identification and a proposal for a new character list, *IAWA J.*, 2015, **36**, 208–241.

62 D. Capitani, V. Di Tullio and N. Proietti, Nuclear magnetic resonance to characterize and monitor cultural heritage, *Prog. Nucl. Magn. Reson. Spectrosc.*, 2012, **64**, 29–69.

63 E. D. Becker, J. A. Ferretti, R. K. Gupta and G. H. Weiss, The choice of optimal parameters for measurement of

spin-lattice relaxation times. II. Comparison of saturation recovery, inversion recovery, and fast inversion recovery experiments, *J. Magn. Reson.*, 1980, **37**, 381–394.

64 R. L. Vold, J. S. Waugh, M. P. Klein and D. E. Phelps, Measurement of spin relaxation in complex systems, *J. Chem. Phys.*, 1968, **48**, 3831–3832.

65 V. V. Krishnan and N. Murali, Radiation damping in modern NMR experiments: Progress and challenges, *Prog. Nucl. Magn. Reson. Spectrosc.*, 2013, **68**, 41–57.

66 S. Meiboom and D. Gill, Modified spin-echo method for measuring nuclear relaxation times, *Rev. Sci. Instrum.*, 1958, **29**, 688–691.

67 R. Amador-Baheza, E. Sacristan-Rock and A. O. Rodríguez, Dual Frequency Coil Array for MR Imaging, *AIP Conf. Proc.*, 2002, **630**, 153–163.

68 A. Haase, Principles and applications of FLASH NMR imaging, *Magn. Reson. Mater. Phys., Biol. Med.*, 1994, **2**, 157–160.

69 H. T. Edzes, D. van Dusschoten and H. Van As, Quantitative T2 imaging of plant tissues by means of multi-echo MRI microscopy, *Magn. Reson. Imaging*, 1998, **16**, 185–196.

70 J. E. Tanner, Use of the stimulated echo in nmr diffusion studies, *J. Chem. Phys.*, 1970, **52**, 2523–2526.

71 D. A. Faux and P. J. McDonald, Nuclear-magnetic-resonance relaxation rates for fluid confined to closed, channel, or planar pores, *Phys. Rev. E*, 2018, **98**, 063110.

72 M. Urbańczyk, A. Shchukina, D. Gołowicz and K. Kazimierczuk, TReNDS—Software for reaction monitoring with time-resolved non-uniform sampling, *Magn. Reson. Chem.*, 2019, **57**, 4–12.

73 P. Galvosas and P. T. Callaghan, Multi-dimensional inverse Laplace spectroscopy in the NMR of porous media, *C. R. Phys.*, 2010, **11**, 172–180.

74 L. Venkataramanan, Y. Q. Song and M. D. Hürlimann, Solving Fredholm integrals of the first kind with tensor product structure in 2 and 2.5 dimensions, *IEEE Trans. Signal Process.*, 2002, **50**, 1017–1026.

75 P. Berman, O. Levi, Y. Parmet, M. Saunders and Z. Wiesman, Laplace inversion of low-resolution NMR relaxometry data using sparse representation methods, *Concepts Magn. Reson., Part A: Bridging Educ. Res.*, 2013, **42**, 72–88.

76 M. Urbańczyk, D. Bernin, W. Koźmiński and K. Kazimierczuk, Iterative thresholding algorithm for multiexponential decay applied to PGSE NMR data, *Anal. Chem.*, 2013, **85**, 1828–1833.

77 A. V. Anisimov, N. Y. Sorokina and N. R. Dautova, Water diffusion in biological porous systems: A NMR approach, *Magn. Reson. Imaging*, 1998, **16**, 565.

78 L. L. Latour, P. P. Mitra, R. L. Kleinberg and C. H. Sotak, Time-Dependent Diffusion Coefficient of Fluids in Porous Media as a Probe of Surface-to-Volume Ratio, *J. Magn. Reson., Ser. A*, 1993, **101**, 342–346.

79 P. P. Mitra, P. N. Sen, L. M. Schwartz and P. Le Doussal, Diffusion propagator as a probe of the structure of porous media, *Phys. Rev. Lett.*, 1992, **68**, 3555.

80 R. W. Mair, P. N. Sen, M. D. Hürlimann, S. Patz, D. G. Cory and R. L. Walsworth, The narrow pulse approximation and long length scale determination in xenon gas diffusion NMR studies of model porous media, *J. Magn. Reson.*, 2002, **156**, 202–212.

81 P. N. Sen, Time-dependent diffusion coefficient as a probe of geometry, *Concepts Magn. Reson., Part A: Bridging Educ. Res.*, 2004, **23A**, 1–21.

82 F. A. L. Dullien, *Porous media: fluid transport and pore structure*, Academic press, 1st edn, 1979.

83 M. Zecca, S. J. Vogt, P. R. J. Connolly, E. F. May and M. L. Johns, NMR Measurements of Tortuosity in Partially Saturated Porous Media, *Transp. Porous Media*, 2018, **125**, 271–288.

84 M. Urbańczyk, Y. Kharbanda, O. Mankinen and V. V. Telkki, Accelerating Restricted Diffusion NMR Studies with Time-Resolved and Ultrafast Methods, *Anal. Chem.*, 2020, **92**, 9948–9955.

85 C. R. Brodersen, Visualizing wood anatomy in three dimensions with high-resolution X-ray micro-tomography (MCT) – A review, *IAWA J.*, 2013, **34**, 408–424.

86 J. Mitchell, J. B. W. Webber and J. H. Strange, Nuclear magnetic resonance cryoporometry, *Phys. Rep.*, 2008, **461**, 1–36.

87 O. Petrov and I. Furó, Curvature-dependent metastability of the solid phase and the freezing-melting hysteresis in pores, *Phys. Rev. E: Stat., Nonlinear, Soft Matter Phys.*, 2006, **73**, 11608.

88 J. H. Strange, M. Rahman and E. G. Smith, Characterization of porous solids by NMR, *Phys. Rev. Lett.*, 1993, **71**, 3589.

89 B. Cowan, *Nuclear Magnetic Resonance and Relaxation*, 1997.

90 Y. Kharbanda, M. Urbańczyk, O. Laitinen, K. Kling, S. Pallaspuro, S. Komulainen, H. Liimatainen and V.-V. Telkki, Comprehensive NMR Analysis of Pore Structures in Superabsorbing Cellulose Nanofiber Aerogels, *J. Phys. Chem. C*, 2019, **123**, 30986–30995.

91 V. V. Telkki, M. Yliniemi and J. Jokisaari, Moisture in softwoods: Fiber saturation point, hydroxyl site content, and the amount of micropores as determined from NMR relaxation time distributions, *Holzforschung*, 2013, **67**, 291–300.

92 R. S. Menon, A. L. MaCkay, J. R. T. Hailey, M. Bloom, A. E. Burgess and J. S. Swanson, An NMR determination of the physiological water distribution in wood during drying, *J. Appl. Polym. Sci.*, 1987, **33**, 1141–1155.

93 N. Labbé, B. De Jéso, J. C. Lartigue, G. Daudé, M. Pétraud and M. Ratier, Time-domain 1H NMR characterization of the liquid phase in greenwood, *Holzforschung*, 2006, **60**, 265–270.

94 S. Flibotte, R. S. Menon and A. L. MacKay, and J. R. T. Hailey, Proton Magnetic Resonance of Western Red Cedar, *Wood Fiber Sci.*, 2007, **22**, 362–376.

95 K. R. Brownstein, Diffusion as an explanation of observed NMR behavior of water absorbed on wood, *J. Magn. Reson.*, 1980, **40**, 505–510.

96 C. Cai, F. Zhou and J. Cai, Bound water content and pore size distribution of thermally modified wood studied by nmr, *Forests*, 2020, **11**, 1279.

97 M. Fredriksson and P. Johansson, A Method for Determination of Absorption Isotherms at High Relative Humidity

Levels: Measurements on Lime-Silica Brick and Norway Spruce (Picea abies (L.) Karst, *Dry. Technol.*, 2016, **34**, 132–141.

98 M. Fredriksson and L. G. Thygesen, The states of water in Norway spruce (Picea abies (L.) Karst.) studied by low-field nuclear magnetic resonance (LFNMR) relaxometry: Assignment of free-water populations based on quantitative wood anatomy, *Holzforschung*, 2017, **71**, 77–90.

99 C. Capretti, N. Macchioni, B. Pizzo, G. Galotta, G. Giachi and D. Giampaola, The characterization of waterlogged archaeological wood: The three roman ships found in Naples (Italy), *Archaeometry*, 2008, **50**, 855–876.

100 P. O. Kettunen, *Wood Structure and Properties*, Trans Tech Publications, Uetikon-Zuerich, 2006.

101 R. S. Menon, A. L. Mackay, S. Flibotte and J. R. T. Hailey, Quantitative separation of NMR images of water in wood on the basis of T2, *J. Magn. Reson.*, 1989, **82**, 205–210.

102 K. R. Brownstein and C. E. Tarr, Importance of classical diffusion in NMR studies of water in biological cells, *Phys. Rev. A*, 1979, **19**, 2446.

103 L. Han, X. Tian, T. Keplinger, H. Zhou, R. Li, K. Svedström, I. Burgert, Y. Yin and J. Guo, Even visually intact cell walls in waterlogged archaeological wood are chemically deteriorated and mechanically fragile: A case of a 170 year-old shipwreck, *Molecules*, 2020, **25**, 1113.

104 J. Guo, J. Chen, R. Li, J. Liu, R. Luo, L. Jiao and Y. Yin, Thermoporometry of waterlogged archaeological wood: Insights into the change of pore traits after the water-removal by supercritical drying, *Thermochim. Acta*, 2022, **715**, 179297.

105 H. Cao, X. Gao, J. Chen, G. Xi, Y. Yin and J. Guo, Changes in Moisture Characteristics of Waterlogged Archaeological Wood Owing to Microbial Degradation, *Forests*, 2023, **14**, 9.